

# Anisotropic Diffusion in Mesh-Free Numerical Magnetohydrodynamics

Philip F. Hopkins<sup>1</sup>\*

<sup>1</sup>TAPIR & The Walter Burke Institute for Theoretical Physics, Mailcode 350-17, California Institute of Technology, Pasadena, CA 91125, USA

Submitted to MNRAS, January, 2016

## ABSTRACT

We extend recently-developed mesh-free Lagrangian methods for numerical magnetohydrodynamics (MHD) to arbitrary anisotropic diffusion equations, including: passive scalar diffusion, Spitzer-Braginskii conduction and viscosity, cosmic ray diffusion/streaming, anisotropic radiation transport, non-ideal MHD (Ohmic resistivity, ambipolar diffusion, the Hall effect), and turbulent “eddy diffusion.” We study these as implemented in the code GIZMO for both new meshless finite-volume Godunov schemes (MFM/MFV) as well as smoothed-particle hydrodynamics (SPH). We show the MFM/MFV methods are accurate and stable even with noisy fields and irregular particle arrangements, and recover the correct behavior even in arbitrarily anisotropic cases. They are competitive with state-of-the-art AMR/moving-mesh methods, and can correctly treat anisotropic diffusion-driven instabilities (e.g. the MTI and HBI, Hall MRI). We also develop a new scheme for stabilizing anisotropic tensor-valued fluxes with high-order gradient estimators and non-linear flux limiters, which is trivially generalized to AMR/moving-mesh codes. We find that SPH is accurate for isotropic diffusion; however, fundamental errors in the most common SPH discretizations are either numerically unstable, or produce large systematic errors in anisotropic cases that do not converge. We develop a new integral-Godunov SPH formulation which resolves these errors by replacing the standard SPH gradient estimator with a moving least-squares estimator and solving a flux-limited Riemann problem between particles. However in problems with full MHD, well-known SPH errors can still swamp the physical diffusivity.

**Key words:** methods: numerical — hydrodynamics — MHD — instabilities — conduction — diffusion

## 1 INTRODUCTION

Diffusion operators are ubiquitous in physical systems, manifest in e.g. conduction, viscosity, cosmic ray diffusion/streaming, photon diffusion (in optically thick media), sub-grid “turbulent eddy” diffusion, passive scalar (e.g. metal) diffusion, Ohmic resistivity, ambipolar diffusion, the Hall effect, and more. Most of these are fundamentally anisotropic. Magnetic fields, fluid flow, or radiation flux can all break isotropy and introduce a (local) preferred direction. The effects are large – for the same initial conditions but different magnetic field configurations, effects like viscosity or conduction might dominate the hydrodynamics, or be completely suppressed. Moreover, anisotropy can introduce qualitatively new behaviors and physical instabilities (e.g. Balbus 2000; Quataert 2008).

Clearly, it is important to capture these phenomena accurately in numerical simulations. In regular, non-moving mesh methods (including fixed-grid and adaptive mesh-refinement [AMR]), the properties of diffusion equations are reasonably well-understood, but even in these cases it is highly non-trivial to formulate anisotropic operators in a numerically stable fashion (see, e.g. Sharma & Hammett 2007). But for some classes of problems, these methods are sub-optimal. They tend to produce excessive diffusion when a fluid is moving rapidly relative to the grid, especially across contact discontinuities (Tasker & Bryan 2008; Springel 2010; Hopkins 2015b); have difficulty coupling to N-body gravity methods and handling self-gravitating hydrostatic equilibrium (Müller & Steinmetz 1995; LeVeque 1998; Zingale et al. 2002); introduce low-order errors around refinement boundaries (O’Shea et al. 2005; Heitmann et al. 2008); and feature inherently preferred directions which can introduce systematic errors even at high resolution if physical anisotropies are not aligned with the grid axes (e.g. Peery

& Imlay 1988; Hahn et al. 2010; Hopkins 2015b; Hopkins & Raives 2016).

Mesh-free methods can avoid these sources of error, and so are popular for many problems in astrophysics. However, the most popular mesh-free method, smoothed-particle hydrodynamics (SPH) has its own difficulties. For example, SPH requires the use of artificial diffusion operators to maintain numerical stability, which can produce excessive numerical viscosity and over-smoothing of shocks and discontinuities (Cullen & Dehnen 2010); tends to suppress fluid-mixing instabilities (Morris 1996; Ritchie & Thomas 2001; Agertz et al. 2007); and suffer from zeroth-order errors (“E0” errors Morris 1996; Dils 1999; Read et al. 2010) which produce systematic errors that do not converge with resolution alone. Although there have been improvements in all of these (see Hopkins 2013; Rosswog 2014; Hu et al. 2014), the E0 errors cannot be completely eliminated from SPH without making the method numerically unstable (Price 2012).

Recently, however, Lanson & Vila (2008a,b); Gaburov & Ntadori (2011); Hopkins (2015b) have developed a class of new, mesh-free Lagrangian finite-volume methods which are both high-order consistent and fully conservative. Similar to moving-mesh codes (Springel 2010; Duffell & MacFadyen 2011; Gaburov et al. 2012), these new methods appear to capture many of the advantages of AMR and SPH, while avoiding the disadvantages above (although, of course, they feature their own sources of error such as enhanced “grid noise” and volume “partition noise”; see Hopkins 2015b). In Hopkins 2015b (hereafter Paper I) and Hopkins & Raives (2016) (Paper II), these are developed for magnetohydrodynamics (MHD) in the multi-method code GIZMO.<sup>1</sup>

<sup>1</sup> GIZMO is a multi-method magnetohydrodynamics+gravity+cosmology code, built on the N-body gravity and domain decomposition algorithms from GADGET-3 (Springel 2005). It includes a variety of optional hydro-

\* E-mail: phopkins@caltech.edu

In this paper, therefore, we extend these new methods and “improved SPH” to include arbitrary anisotropic diffusion operators. We consider a systematic comparison of the methods, in order to determine the degree of anisotropy that can be reliably treated. Moreover we consider a variety of possible discretizations of SPH diffusion operators, and examine how they perform under different circumstances.

## 2 GENERAL DIFFUSION OPERATORS IN MESHLESS FINITE-VOLUME GODUNOV METHODS

The general diffusion equation in conservative form is:

$$\frac{d\mathbf{U}}{dt} = -\nabla \cdot \mathbf{F}_{\text{diff}} \quad (1)$$

$$\mathbf{F}_{\text{diff}} = -\mathbf{K} \cdot (\nabla \otimes \mathbf{q}) \quad (2)$$

where  $d/dt$  is a Lagrangian derivative, and  $\mathbf{F}_{\text{diff}}$  a diffusive flux given by a linear combination of the tensor field  $\mathbf{K}$  and the gradients of the field  $\mathbf{q}$ . We denote the inner product  $\cdot$  and outer product  $\otimes$ .

In the mesh-free finite-volume or finite-mass (MFV or MFM, respectively) formulations of the Lagrangian methods in Gaburov & Nitadori (2011) and Paper I, we begin from a general conservation equation of the form  $D\mathbf{U}/Dt = -\nabla \cdot \mathbf{F}$  and use this to derive a second-order accurate Godunov-type numerical expression of the hydrodynamic equations. It is therefore trivial to apply the same here, giving

$$\frac{d}{dt}(V\mathbf{U})_i = -\sum_j \mathbf{F}_{\text{diff},ij}^* \cdot \mathbf{A}_{ij} \quad (3)$$

where  $\mathbf{A}_{ij}$  is the “effective face area” (defined in Paper I; it depends on the inter-element spacing and kernel shape, and reduces to the geometric faces of a Voronoi tessellation in the limit of a delta-function kernel). The same would obtain for Cartesian grid methods and moving-mesh codes, with  $\mathbf{A}_{ij}$  the usual inter-face area. Here  $\mathbf{F}_{\text{diff},ij}^*$  is the *interface* value of the flux.

The solution then follows our usual MHD method: we calculate the coefficients, perform a reconstruction step to estimate quantities “at the face,” replace the flux with the solution to a Riemann problem (RP), and use this to update the conserved quantities. We will explain this in more detail below.

Note that Eq. 3 is manifestly antisymmetric, so conserved quantities ( $V\mathbf{U}$ ) are manifestly conserved as desired.

Additionally, we note that the MFM and MFV methods from Paper I differ only at second order in how they handle advection between particles. In diffusion-only problems, they are manifestly identical. Therefore, we do not show both (although we have confirmed their identical results), but will, for simplicity, adopt MFM as our reference method.

### 2.1 Gradient Estimation & Reconstruction

We require gradients for all quantities; to do this, we adopt the standard gradient estimator in GIZMO, a moving, second-order accurate

dynamic methods, including the meshless finite-mass (MFM) and finite-volume (MFV) schemes from Paper I, but also state-of-the-art implementations of SPH. A public version of the code is available at <http://www.tapir.caltech.edu/~phopkins/Site/GIZMO.html>. Users are encouraged to modify and extend the code.

and consistent least-squares estimator. For a scalar  $f$ , this is

$$(\nabla f)_i^\alpha = \sum_j (f_j - f_i) \left( \mathbf{W}_i^{-1} \right)^{\alpha\beta} (\mathbf{x}_j - \mathbf{x}_i)^\beta \omega_j(\mathbf{x}_i) \quad (4)$$

$$\mathbf{W}_i^{\alpha\beta} \equiv \sum_j (\mathbf{x}_j - \mathbf{x}_i)^\alpha (\mathbf{x}_j - \mathbf{x}_i)^\beta \omega_j(\mathbf{x}_i) \quad (5)$$

here we assume an Einstein summation convention over the indices  $\beta$  corresponding to the spatial dimensions, and  $\omega_j(\mathbf{x}_i)$  is an (arbitrary) weight function defined in Paper I. This estimator is second-order accurate for an *arbitrary* mesh/particle configuration, minimizes the (weighted) least-squares deviation  $\sum_j \omega_j |f_i + \nabla f_i \cdot (\mathbf{x}_j - \mathbf{x}_i) - f_j|^2$ , and has been applied in a wide range of different numerical methods (see e.g. Oñate et al. 1996; Kuhnert 2003; Maron & Howes 2003; Luo et al. 2008; Lanson & Vila 2008a). Note that Eq. 4 applies to a scalar field  $f$ . For a general tensor  $\mathbf{q}$ , we apply Eq. 4 separately to every component  $f = q_{\alpha\beta\gamma\dots}$  to determine all partial derivatives needed to construct  $\nabla \otimes \mathbf{q}$  and  $\mathbf{F}_{\text{diff}}$ . The gradients are slope-limited as described in Paper I, such that they do not create new local extrema within the interacting kernel.

In the reconstruction step we must extrapolate the values from  $i$  and  $j$  to the left and right sides of the face. For hydrodynamics and MHD, we perform a linear reconstruction of all the MHD quantities based on their slope-limited gradients (see Paper I). For additional quantities needed for diffusion, our default approach is a first-order reconstruction, e.g.  $(\nabla \otimes \mathbf{q})_{R,L} = (\nabla \otimes \mathbf{q})_{i,j}$ . This is easy to implement, and most stable, but comes at the cost of greater numerical diffusion. We have therefore also considered limited tests using the “double linear” reconstruction of Muñoz et al. (2013). This amounts to treating  $\nabla \otimes \mathbf{q}$  like any other primitive variable. In a first loop, we calculate  $\nabla \otimes \mathbf{q}$  with our standard method; in a second loop, we calculate  $\nabla \otimes (\nabla \otimes \mathbf{q})$ , and use this to linearly reconstruct  $(\nabla \otimes \mathbf{q})_{R,L}$  (or any component of it) like any other primitive variable. This gives a simple, second-order Taylor-series representation which implicitly includes an appropriately larger stencil (since the second pass sums over the values  $(\nabla \otimes \mathbf{q})_j$ , themselves constructed from the  $\mathbf{q}_k$  in all neighbors of  $j$ ). To ensure smoothness, the reconstructed gradients in the double-linear method are slope-limited with respect to the particle-centered gradients using the same limiter we adopt for all the usual MHD quantities (see Paper I).

### 2.2 The Riemann Problem

We treat diffusion in operator-split fashion from the pure-MHD RP. We have experimented with several Riemann solvers for the diffusion RP, and find the best compromise between numerical diffusion, stability, and flexibility using the Harten et al. (1983) (HLL) solver in the Lagrangian frame. In this case:

$$\mathbf{F}_{\text{diff},ij}^* = \frac{\lambda^+ \mathbf{F}_{\text{diff},L} - \lambda^- \mathbf{F}_{\text{diff},R} + \alpha \lambda^+ \lambda^- (\mathbf{U}_R - \mathbf{U}_L)}{\lambda^+ - \lambda^-} \quad (6)$$

where the maximum/minimum wavespeeds  $\lambda^+/\lambda^-$  are determined appropriate to the problem. Here  $\mathbf{U}_R, \mathbf{U}_L$  are the appropriate right/left states reconstructed at the face following Paper I (extrapolated from the particle-centered values to the face with the derivatives of  $\mathbf{U}$ , with a MINMOD slope limiter).

Consider the case where we are using our second-order reconstruction in a Lagrangian frame. We adopt the wavespeed estimate from Paper I,  $\lambda^+ = \text{MAX}(v_L, v_R) + c_{\text{fast}}$ ,  $\lambda^- = \text{MIN}(v_L, v_R) - c_{\text{fast}}$ . Here  $c_{\text{fast}}$  is a fastest wavespeed determined by the 1D RP. Then, because in our default GIZMO method our frame is moving with  $v = (v_L + v_R)/2$ , in the Lagrangian frame we simply obtain  $\lambda^+ =$

$-\lambda^{-1} = |v_R - v_L|/2 + c_{\text{fast}}$ , in which case the HLL solution reduces to the Global Lax Friedrich (GLF) function:  $\mathbf{F}_{\text{diff},ij}^* = (\mathbf{F}_{\text{diff},L} + \mathbf{F}_{\text{diff},R})/2 - \alpha (|v_R - v_L|/2 + c_{\text{fast}}) (\mathbf{U}_R - \mathbf{U}_L)/2$ .

Although using the GLF flux in *non*-Lagrangian methods tends to be excessively diffusive, here it gives nearly indistinguishable results from using the HLL solution with another wavespeed estimate (e.g. Roe wavespeeds or the exact eigenvalues of the Jacobian  $\partial\mathbf{F}/\partial\mathbf{U}$ ). This is because the first-order term owing to frame motion is automatically accounted for by the Lagrangian nature of the method. Even if we use a double-linear reconstruction, we see only a tiny (percent-level) increase in diffusion using this particular form for the RP solution.

Using the above with  $\alpha = 1$  gives an effective numerical diffusivity  $\kappa_n \sim c_s |\mathbf{x}|_{ij}$ , which can easily exceed the physical  $\kappa_p$  by large factors at low resolution. We prevent this by replacing Eq. 6 with the flux-limited equation:

$$\mathbf{F}_{\text{HLL}} = \text{MINMOD}((1 + \psi)\mathbf{F}_2, \mathbf{F}_2 + \mathbf{F}_U) \quad (7)$$

$$\mathbf{F}_2 = \frac{\lambda^+ \mathbf{F}_{\text{diff},L} - \lambda^- \mathbf{F}_{\text{diff},R}}{\lambda^+ - \lambda^-} \quad (8)$$

$$\mathbf{F}_U \equiv \alpha \left[ \frac{\lambda^+ \lambda^- (\mathbf{U}_R - \mathbf{U}_L)}{\lambda^+ - \lambda^-} \right] \quad (9)$$

$$\alpha \equiv \left( \frac{\|\mathbf{K}^* \cdot (\nabla \otimes \mathbf{q})^*\|}{\|\mathbf{K}^*\| \|(\nabla \otimes \mathbf{q})^*\|} \right) \left( \frac{0.2 + r}{0.2 + r + r^2} \right) \quad (10)$$

$$r \equiv \left( \frac{|v_R - v_L|}{2} + c_{\text{fast}}^* \right) \frac{\|\mathbf{x}_j - \mathbf{x}_i\| \|\mathbf{q}^*\|}{\|\mathbf{K}^*\| \|\mathbf{U}^*\|} \quad (11)$$

where above  $\mathbf{F}_2$  is the flux we would obtain in the simplest 2nd-order accurate (but numerically unstable) formulation.  $\mathbf{F}_U$  is the diffusive flux from the Riemann problem, appropriately limited by the function  $\alpha$ . Here  $\|\mathbf{x}\|$  refers to the Frobenius norm of the tensor  $\mathbf{x}$ , and  $f^*$  refers to the interface value of the primitive variable  $f$ ; where possible we adopt these from the appropriate solution to the pure-MHD RP, otherwise we approximate  $f^* = (f_L + f_R)/2$ .

The first term in  $\alpha$  (in  $\mathbf{K}$  and  $\nabla \otimes \mathbf{q}$ ) limits  $\mathbf{F}_U$  for the anisotropic case,<sup>2</sup> vanishing as  $F_{\text{diff}}$  does where there is full anisotropic suppression (even at low resolution).

The second term in  $\alpha$  ensures  $\alpha \rightarrow 1$  at small  $r$  and  $\alpha \rightarrow 1/r$  at large  $r$  (the functional form is motivated by Rosdahl & Teyssier 2015); together with the MINMOD application this prevents the numerical diffusivity from exceeding physical values by more than some tolerance parameter  $\psi$ . As usual this parameter represents some tradeoff: increasing  $\psi$  gives smoother solutions at the expense of numerical diffusivity. We find our qualitative results are robust for all  $0.05 < \psi < 1$ , and use  $\psi = 0.1$  as our default.

Finally, we also compute a “direct” flux based on pairwise

direct-difference gradients, and use this to restrict  $\mathbf{F}_{\text{diff},ij}^*$  via:

$$(\mathbf{F} \cdot \mathbf{A})_{\text{direct}} \equiv - \left[ \frac{\mathbf{K}_i + \mathbf{K}_j}{2} \cdot (\nabla \otimes \mathbf{q})_{\text{dir}} \right] \cdot \|\mathbf{A}_{ij}\| \frac{\mathbf{x}_j - \mathbf{x}_i}{\|\mathbf{x}_j - \mathbf{x}_i\|} \quad (12)$$

$$(\nabla \otimes \mathbf{q})_{\text{dir}} \equiv \frac{(\mathbf{x}_j - \mathbf{x}_i) \otimes (\mathbf{q}_j - \mathbf{q}_i)}{\|\mathbf{x}_j - \mathbf{x}_i\|^2} \quad (13)$$

$$\mathbf{F}_{\text{diff},ij}^* = \begin{cases} \mathbf{0} & (\text{SIGN}[(\mathbf{F} \cdot \mathbf{A})_{\text{direct}}] \neq \text{SIGN}[\mathbf{F}_{\text{HLL}} \cdot \mathbf{A}_{ij}] \\ & \text{and } \|(\mathbf{F} \cdot \mathbf{A})_{\text{direct}}\| > \epsilon \|\mathbf{F}_{\text{HLL}} \cdot \mathbf{A}_{ij}\| \\ \mathbf{F}_{\text{HLL}} & \text{otherwise} \end{cases} \quad (14)$$

with the tolerance parameter  $0 \leq \epsilon \leq 1$ . We find stable (albeit slightly more noisy) results in all our problems using values as large as  $\epsilon = 2$ , in fact, and larger values do give improved performance at low resolution on multi-dimensional tests (e.g. the diffusing ring), but we adopt  $\epsilon = 1/2$  as our default here.

We note that this is not the only way to stabilize the anisotropic diffusion equations. For example, Sharma & Hammett (2007) propose an elegant slope-limiting method; however, it is not obvious how to extend this to unstructured meshes. Recently, Kannan et al. (2015) implemented the method of Gao & Wu (2013) for moving-mesh codes. The advantage of their method is that it is extremum-preserving and generalizes relatively easily to implicit integrators. However, we choose to explore alternatives for three reasons. First, the Gao & Wu (2013) method implicitly uses the lower-order “direct” gradients, as opposed to our (in principle arbitrarily high-order) matrix-based gradient estimator, necessarily making the method lower-order. Moreover in flows where there is a clear mean-field gradient but large resolution-scale noise, matrix-based estimators are significantly more robust (see García-Senz et al. 2012; Mocz et al. 2014; Pakmor et al. 2016). Second, our method here allows for non-linear flux-limiting terms (e.g.  $\alpha$  above) which allow us to limit numerical diffusion to physical values even at arbitrarily low resolution (potentially important in multi-physics problems where the diffusion may, in some places, dominate only on un-resolved scales). And third, our method here, unlike most in the literature, allows for any (arbitrarily complex) tensor  $\mathbf{q}$ , and/or linear combinations of  $\mathbf{K}$  and the elements of  $\nabla \otimes \mathbf{q}$  in the fluxes (relevant for e.g. radiation transport, Braginskii viscosity, and the Hall effect).

### 2.3 Timestepping

In addition to the usual timestep limiters (e.g., the CFL condition, gravitational acceleration-based limiters) which always apply, ensuring stability in explicit methods for diffusion equations requires an additional timestep criterion:

$$\Delta t \leq \frac{1}{\|\mathbf{K}\|} \left[ \frac{\|\nabla \otimes \mathbf{q}\|}{\|\mathbf{q}\|} + \frac{1}{\Delta x} \right]^{-2} \frac{\|\mathbf{U}\|}{\|\mathbf{q}\|} \quad (15)$$

For the simplest diffusion example,  $\partial U / \partial t = \kappa \partial^2 U / \partial x^2$  and an appropriately slope-limited gradient, this reduces to the common expression  $\Delta t \leq \Delta x^2 / \kappa$ . We also require that the inter-particle flux between a particle and any neighbors of the conserved  $V\mathbf{U}$  cannot exceed half the minimum of the  $|V\mathbf{U}|$  in the pair, in a single timestep, but find this criterion is always satisfied if the above (more strict) criterion is as well.

## 3 GENERAL DIFFUSION OPERATORS IN SPH

As described in Paper I & Paper II, GIZMO is a multi-method code: users can run with our meshless Godunov (MFM or MFV) hydrodynamic methods, or SPH, if desired. In this mode, all elements

<sup>2</sup> Note that the form of  $\mathbf{K} \cdot (\nabla \otimes \mathbf{q})$  in Eq. 10 follows directly from the form of  $\mathbf{F}_{\text{diff}} = \mathbf{K} \cdot (\nabla \otimes \mathbf{q})$ . For the cases where  $F_{\text{diff}}$  is represented by a different linear combination of gradients, the term in Eq. 10 should be modified accordingly.

of the code (e.g. integration method, timestepping) are kept fixed, except for the hydro solver, facilitating methods comparisons. We therefore describe the SPH implementation of the same diffusion equations.

### 3.1 The “Standard” SPH Diffusion Operator

SPH is not a finite-volume method; instead of Eq. 3, we have

$$\frac{d}{dt}(V\mathbf{U})_i^{\text{SPH}} = -\frac{m_i}{\rho_i}(\nabla \cdot \mathbf{F}_{\text{diff}})_i = \frac{m_i}{\rho_i} \{ \nabla \cdot [\mathbf{K} \cdot (\nabla \otimes \mathbf{q})] \}_i \quad (16)$$

Note some differences. (1) This does not compute a volume-integral of  $d\mathbf{U}/dt$  (as in Godunov methods), but approximates it by multiplying the value of  $d\mathbf{U}/dt$  at the particle center-of-mass by an effective volume  $m_i/\rho_i$ . (2) There is no RP. (3) It requires we evaluate numerical second derivatives of  $\mathbf{q}$ .

This last point is especially challenging. Various groups have adopted generalizations of the integral-based, hybrid derivatives first proposed in Brookshaw (1985). Español & Revenga (2003), Petkova & Springel (2009) and Arth et al. (2014) all present detailed derivations beginning from the Taylor expansion of  $\mathbf{q}$  and using the same moments-based integral approach to compute the mixed tensor derivatives, and arrive at identical expressions which minimize the integral of the leading-order SPH errors in the continuum limit (what we refer to as the “error-corrected” formulation below; § 3.2.3). However both Petkova & Springel (2009) and Arth et al. (2014) immediately note this is unstable for sufficiently anisotropic problems (Español & Revenga (2003) did not consider this case), and derive the minimum correction (adding an artificial dissipation term in analogy to the SPH artificial viscosity) required to stabilize the equation. Their final result is:

$$\begin{aligned} \frac{d(V\mathbf{U})_i}{dt} &= \frac{m_i}{\rho_i} \sum_j \frac{m_j}{\rho_j} \mathbf{x}_{ij}^T \left[ \frac{\mathbf{K}_j + \mathbf{K}_i}{|\mathbf{x}_{ij}^2|} \right] \quad (17) \\ &\left[ \frac{(\nabla_i W_{ij} + \nabla_j W_{ij})}{2} \otimes (\mathbf{q}_j - \mathbf{q}_i) \right] \\ &= \sum_j \frac{m_i m_j}{\rho_i \rho_j} \frac{\tilde{W}_{ij}}{|\mathbf{x}_{ij}|} \{ \hat{\mathbf{x}}_{ij}^T [(\mathbf{K}_j + \mathbf{K}_i) (\hat{\mathbf{x}}_{ij} \otimes [\mathbf{q}_j - \mathbf{q}_i])] \} \\ \tilde{W}_{ij} &\equiv \frac{1}{2} \left[ \frac{\partial W(|\mathbf{x}_{ij}|/h_i, h_i)}{\partial |\mathbf{x}_{ij}|} + \frac{\partial W(|\mathbf{x}_{ij}|/h_j, h_j)}{\partial |\mathbf{x}_{ij}|} \right] \quad (18) \end{aligned}$$

where  $\mathbf{x}_{ij} = \mathbf{x}_i - \mathbf{x}_j$ . Note that generalizing this to any linear combination of gradients of  $\mathbf{q}$  is straightforward (as needed for e.g. anisotropic viscosity and radiation transport); we replace the  $\hat{\mathbf{x}} \otimes \mathbf{q}$  term above (which represents  $\nabla \otimes \mathbf{q}$ ) with the desired linear combination of itself and/or  $\hat{\mathbf{x}} \cdot \mathbf{q}$  representing  $\nabla \cdot \mathbf{q}$  (or  $\hat{\mathbf{x}} \times \mathbf{q}$  for  $\nabla \times \mathbf{q}$ ).<sup>3</sup> If  $\mathbf{q} = q$  is a scalar, this simplifies to

$$\frac{d(VU)_i}{dt} \rightarrow \sum_j \frac{m_i m_j}{\rho_i \rho_j} \frac{(q_j - q_i)}{|\mathbf{x}_{ij}|} \tilde{W}_{ij} [\hat{\mathbf{x}}_{ij}^T (\mathbf{K}_j + \mathbf{K}_i) \hat{\mathbf{x}}_{ij}] \quad (19)$$

For the isotropic case,  $\mathbf{K} = K\mathbf{I}$ , we have  $\hat{\mathbf{x}}_{ij}^T (\mathbf{K}_j + \mathbf{K}_i) \hat{\mathbf{x}}_{ij} = (K_j + K_i)$ , and this reduces to the original expression in Brookshaw (1985). For the magnetic case with  $\mathbf{K} = K\hat{\mathbf{B}} \otimes \hat{\mathbf{B}}$ , we have  $\hat{\mathbf{x}}_{ij}^T (\mathbf{K}_j + \mathbf{K}_i) \hat{\mathbf{x}}_{ij} = K_j |\hat{\mathbf{x}}_{ij} \cdot \hat{\mathbf{B}}|^2 + K_i |\hat{\mathbf{x}}_{ij} \cdot \hat{\mathbf{B}}|^2$ .

<sup>3</sup> Note also that a wide range of subtle variants of Eq. 17 can be easily derived by replacing terms in  $i$  or  $j$  with averages ( $\rho_i \rightarrow (\rho_i + \rho_j)/2$ ) or replacing arithmetic averages with geometric ones ( $K_i + K_j \rightarrow 2K_i K_j / (K_i + K_j)$ ) (see e.g. Cleary & Monaghan 1999; Price 2012). We have experimented with a variety of these and find the differences are small compared to all other methodological choices we explore, so we will not discuss them further.

We will refer to this as the “standard” SPH diffusion operator only because it has thus far been the most popular formulation used for true anisotropic diffusion problems in SPH (see e.g. Petkova & Springel 2009, 2011b,a; Petkova & Maio 2012; Maio et al. 2013; Sales et al. 2013; Arth et al. 2014), and because it reduces for the isotropic, scalar case to the nearly-ubiquitous SPH formulation of Brookshaw (1985). However it is neither the only nor necessarily most accurate SPH approach, as discussed below.

#### 3.1.1 Artificial Numerical Diffusion and Stability

It is straightforward to show that the formulation above is unconditionally stable, without the need for further limiters or numerical diffusion. This follows from the sign of  $\mathbf{q}_j - \mathbf{q}_i$  and the fact that  $\hat{\mathbf{x}}_{ij}^T (\mathbf{K}_j + \mathbf{K}_i) \hat{\mathbf{x}}_{ij}$  is positive-definite.

#### 3.1.2 Low-Order Errors in the Standard SPH Method

This expression has a number of advantages over other possible SPH discretizations. Most importantly, it is numerically stable. It is also manifestly antisymmetric in  $i$  and  $j$ , so conserved quantities ( $V\mathbf{U}$ ) are manifestly conserved. It also involves only first derivatives of the kernel function  $W$ , and can be evaluated in a single SPH pass. And the explicit difference  $\mathbf{q}_j - \mathbf{q}_i$  means that zero diffusion is guaranteed between particles of identical  $\mathbf{q}$ .

It is useful to write Eq. 17 in the finite-volume form of Eq. 3, by making the identification  $-\mathbf{F}_{\text{diff},ij}^* = [\mathbf{K} \cdot (\nabla \otimes \mathbf{q})]^* \rightarrow \frac{1}{2}(\mathbf{K}_i + \mathbf{K}_j) \cdot [(\hat{\mathbf{x}}_{ij}/|\mathbf{x}_{ij}|) \otimes (\mathbf{q}_j - \mathbf{q}_i)]$  and  $\mathbf{A}_{ij} \rightarrow [m_i m_j / (\rho_i \rho_j)] 2\tilde{W}_{ij} \hat{\mathbf{x}} = V_i V_j [\nabla_i W_{ij}(h_i) + \nabla_j W_{ij}(h_j)]$ . Thus we assume an “effective face” between pairs (an identical face appears if we similarly decompose the SPH hydro equations), with area  $\sim V_i V_j |\nabla W|$ , and face orientation along the axis  $\hat{\mathbf{x}}_{ij}$  between each particle pair. Likewise, we approximate  $\nabla q$  by the direct difference  $(q_j - q_i)/|\mathbf{x}_{ij}|$ , assuming the gradient direction also lies along  $\hat{\mathbf{x}}_{ij}$ .

These approximations explain the errors we will see below. Because the gradients and “faces” are assumed to be oriented along  $\hat{\mathbf{x}}_{ij}$ , the results are sensitive the particle arrangement, and systematic errors can appear that do not converge away even for a simple case with uniform flux everywhere. Consider e.g. constant  $\mathbf{K}_i = K\hat{\mathbf{B}} \otimes \hat{\mathbf{B}}$  with  $\hat{\mathbf{B}} = \hat{\mathbf{y}}$  and a uniform gradient  $q_i = q'x_i$ ; the term inside the sum in Eq. 17 becomes  $\sim V_i (Kq') x_{ij} y_{ij}^2 / |\mathbf{x}_{ij}|^4$ . So, unless the particles are distributed exactly isotropically (so cancel exactly), there will be non-zero flux even though  $\mathbf{K} \cdot (\nabla \otimes \mathbf{q}) = 0$  everywhere. Since  $d(VU)_i/dt \sim V_i dU_i/dt$ , we have a contribution to  $dU_i/dt \sim (Kq') x_{ij} y_{ij}^2 / |\mathbf{x}_{ij}|^4 \sim (Kq') |\mathbf{x}_{ij}|^{-1} \sim \mathcal{O}(h^{-1})$ , so the errors do not decrease with increasing resolution.

### 3.2 Alternative Operators

There are alternatives to Eq. 17 within the “standard” SPH context, however we will show these all give either comparable performance or are fundamentally unacceptable (e.g. numerically unstable).

#### 3.2.1 Second Kernel Derivatives

In SPH, a standard first-derivative operator is given by:

$$\langle \nabla \otimes \mathbf{q} \rangle_{a,\text{SPH}}^{\alpha\beta\dots} = \sum_b \frac{m_b}{\Omega_a \rho_a} (\mathbf{q}_b - \mathbf{q}_a)^{\beta\dots} (\nabla_a W_{ab})^\alpha \quad (20)$$

where  $\Omega_a \sim 1$  is a correction term accounting for variations in the smoothing length  $h$  (see Springel & Hernquist 2002); we will generally omit this from our expressions here for clarity. The simplest generalization of this to second derivatives is

$$\nabla^2 q_a^{\text{SPH}} \approx \sum_b \frac{m_b}{\rho_a} (q_b - q_a) \nabla_a^2 W_{ab} \quad (21)$$

But this is almost never used, as it produces unacceptably noisy results (because  $\nabla^2 W_{ab}$  changes sign within the kernel, it must be tremendously well-sampled in all directions to give accurate results Brookshaw 1985; Cleary & Monaghan 1999; Price 2012). Moreover, it is not clear how to rigorously generalize this to the anisotropic case with a variable  $\mathbf{K}$ , since one is not taking a flux-derivative but a direct second-derivative. However we can easily apply this estimator at least for the isotropic, scalar- $q$  case by taking

$$\frac{d(VU)_a^{\text{SPH}}}{dt} \rightarrow \sum_b \frac{m_a m_b}{\rho_a \rho_b} \frac{(q_b - q_a)}{2} \left( \nabla_a^2 W_{ab} + \nabla_b^2 W_{ab} \right) [\hat{\mathbf{x}}_{ab}^T (\mathbf{K}_a + \mathbf{K}_b) \hat{\mathbf{x}}_{ab}] \quad (22)$$

### 3.2.2 “Gradients of Gradients”

Alternatively, we can consider a “gradients of gradients” approach, as in e.g. Sijacki & Springel (2006). First, we apply the first-derivative operator in Eq. 20 to obtain  $\langle \nabla \otimes \mathbf{q} \rangle_{a,\text{SPH}}^{\alpha\beta\dots}$ .

Naively, we would apply the same operator once again, with the usual SPH summation rule, to obtain the diffusion equation:

$$\frac{d(VU)_a^{\text{SPH}}}{dt} \rightarrow \sum_b \frac{m_a m_b}{\rho_a \rho_b} \frac{1}{2} (\nabla_a W_{ab} + \nabla_b W_{ab}) \cdot (\mathbf{K}_b \cdot \langle \nabla \otimes \mathbf{q} \rangle_b - \mathbf{K}_a \cdot \langle \nabla \otimes \mathbf{q} \rangle_a) \quad (23)$$

(Note that we symmetrize the  $\nabla W$  and  $\rho$  terms to allow for different smoothing lengths  $h_a, h_b$  between particles). However, this has a serious problem: the fluxes between particles  $a$  and  $b$  are symmetric, not anti-symmetric. This means the method is non-conservative – in fact, an isolated pair of particles will “bootstrap” themselves to infinite values of  $|\mathbf{q}|$ ! Not surprisingly, if we implement Eq. 23, the errors quickly become catastrophic and our test problems run away to infinite values of  $|\mathbf{q}|$  if there is initial noise, particle disorder, or even un-resolved gradients in  $\mathbf{q}$ .<sup>4</sup>

To avoid this, we must use the alternative (conjugate) derivative operator in the second (outer) gradient:

$$\langle \nabla \nabla \cdot \mathbf{F} \rangle_{a,\text{SPH}}^* = \rho_a \sum_b m_b \left( \frac{\mathbf{F}_a \cdot \nabla_a W_{ab}}{\Omega_a^2 \rho_a^2} + \frac{\mathbf{F}_b \cdot \nabla_b W_{ab}}{\Omega_b^2 \rho_b^2} \right) \quad (24)$$

which gives rise to the diffusion equation from Sijacki & Springel (2006):

$$\frac{d(VU)_a^{\text{SPH}}}{dt} \rightarrow \sum_b m_a m_b \left( \frac{\mathbf{K}_a \cdot \langle \nabla \otimes \mathbf{q} \rangle_a}{\Omega_a^2 \rho_a^2} \cdot \nabla_a W_{ab} + \frac{\mathbf{K}_b \cdot \langle \nabla \otimes \mathbf{q} \rangle_b}{\Omega_b^2 \rho_b^2} \cdot \nabla_b W_{ab} \right) \quad (25)$$

Eq. 25 is manifestly anti-symmetric, so is conservative.<sup>5</sup>

Note that Eq. 25 is the exact formulation used to study isotropic diffusion in Sijacki & Springel (2006); Tsukamoto et al. (2013); Wurster et al. (2014); as well as non-linear simulations with non-ideal MHD (admitting anisotropic terms) in Tsukamoto et al. (2015b,a); Wurster et al. (2016).

Modulo the “weighting factors,” Eq. 24 is identical to Eq. 20

up to the subtraction of  $q_a$  (or  $\mathbf{F}_a$ ) within the sum. Because this term factors out of the sum, the two are identical if  $\rho_a = \rho_b$  and  $\sum_b m_b \rho_b^{-1} \nabla_a W_{ab} = 0$ , i.e. in the continuum limit (infinite number of particles in the kernel). In practice (finite neighbor number), Eq. 24 introduces sub-zeroth-order errors into the estimator, but is necessary to maintain conservation (and stability) in SPH. Note that we can still use the more accurate Eq. 20 to estimate  $\langle \nabla \otimes \mathbf{q} \rangle_{a,\text{SPH}}^{\alpha\beta\dots}$ .

However, three problems remain. **(1)** Eq. 20 still features systematic errors in the gradient that depend on the local particle arrangement.<sup>6</sup> **(2)** Even if the true gradient is perfectly recovered by Eq. 20, Eq. 25 features two zeroth-order systematic errors. **(3)** Eq. 25 is numerically unstable; there is no guarantee heat flows from hot to cold, if (in e.g. a noisy flow) a pair of particles has a pairwise difference in  $\mathbf{q}$  which is opposite the sign of the local gradient.<sup>7</sup>

Restoring stability **(3)** requires some combination of numerical diffusion and/or limiters. We have therefore explored several dozen combinations and find (not surprisingly) the best results using a flux-limiter similar to that used for our MFM method.

The systematic errors **(1)** and **(2)**, however, converge away only with increasing SPH neighbor number (not resolution), as  $\mathcal{O}(N^{-1/2})$  (for a Poisson-like particle distribution) where  $N$  is the number of neighbors in the Gaussian core of the kernel (which increases more slowly than the “total” particle number in the kernel). So going from a 32-neighbor cubic spline (as in our MFM method) to a 400-neighbor Wendland  $C^6$  kernel (see Dehnen & Aly 2012) allows the maximum anisotropy which can be captured to increase from a factor  $\sim 4$  to factor  $\sim 9$ .

### 3.2.3 “Error-Corrected” Formulations

As noted above, both Petkova & Springel (2009) and Arth et al. (2014), in attempting to derive a higher-order consistent SPH for-

<sup>6</sup> Consider a locally-constant gradient along the  $\hat{x}$ -axis,  $\nabla q_{\text{true}} = q' \hat{x}$ , and for simplicity assume the particle masses/densities/smoothing lengths are constant within the kernel. Eq. 24 recovers:

$$\langle \nabla q \rangle_{\text{SPH}} = 2q_a \sum_b \frac{m_b}{\rho_b} \frac{\mathbf{x}_{ba}}{|\mathbf{x}_{ba}|} \bar{W}_{ab} + q' \sum_b \frac{m_b}{\rho_b} \hat{x} \cdot \mathbf{x}_{ba} \frac{\mathbf{x}_{ba}}{|\mathbf{x}_{ba}|} \bar{W}_{ab} \quad (26)$$

where  $\mathbf{x}_{ba} \equiv \mathbf{x}_b - \mathbf{x}_a$ . The  $q_a$  term vanishes if we use Eq. 20, but otherwise returns an error  $\mathcal{O}(q_a/h) \sim \mathcal{O}(h^{-1})$ . The  $q'$  error (difference between the coefficient of  $q'$  and unity) is a systematic multiplicative error of  $\mathcal{O}(q') \sim \mathcal{O}(h^0)$ . So, even if we use Eq. 20 for  $\langle \nabla q \rangle$ ,  $\mathbf{K} = \mathbf{K}\mathbf{I}$  is constant, and  $q = q_a + q'(x - x_a) + q''(x - x_a)^2$ , then Eq. 25 returns

$$\frac{dU}{dt} = K \left[ 2q' \sum_b \frac{m_b}{\rho_b} \frac{\hat{x} \cdot \mathbf{x}_{ba}}{|\mathbf{x}_{ba}|} \bar{W}_{ab} + q'' \sum_b \frac{m_b}{\rho_b} \frac{|\hat{x} \cdot \mathbf{x}_{ba}|^2}{|\mathbf{x}_{ba}|} \bar{W}_{ab} \right] \quad (27)$$

so there is an error  $\mathcal{O}(2q'/h)$  and another  $\mathcal{O}(q'')$ .

<sup>7</sup> To see this, consider the simple case with  $m, \rho, h, \mathbf{K} = \kappa \hat{\mathbf{B}} \otimes \hat{\mathbf{B}}$ ,  $\hat{\mathbf{B}} = \hat{x}$  all constant, scalar  $\mathbf{U} = \mathbf{q} = u$ ; then Eq. 25 becomes  $\dot{u}_a = \mu \sum_b \epsilon_{ab} x_{ab} (\langle \partial_x u \rangle_a + \langle \partial_x u \rangle_b)$  where  $\epsilon_{ab} \equiv \bar{W}_{ab}/|\mathbf{x}_{ab}|$  and  $\mu = \kappa(m/\rho)$  are positive-definite. For any derivative  $\partial_x u$ , the particle configuration around “ $a$ ” can (in principle) change the sign of  $\dot{u}_a$ . For the especially simple case  $\langle \partial_x u \rangle_{a,b} = \partial_x u = \text{constant}$ , then  $\dot{u}_a = \mu (\partial_x u) \sum_b \epsilon_{ab} x_{ab}$ , i.e. the sign of  $du_a/dt$  is determined by the sign of  $\sum_b \epsilon_{ab} x_{ab}$ , which depends only on the particle arrangement (not on  $u$ ) and can, for different particle arrangements, have either sign. Therefore it is always possible to find a particle arrangement such that the sign of  $\sum_b \epsilon_{ab} x_{ab}$  ensures a net flux from low  $u$  to high  $u$  (i.e. hot-to-cold). More generally, the formulation of Eq. 25 is always locally unstable (allows hot-to-cold flux between individual particle pairs); but it is globally stable (the net flux, summed over all neighbors, is guaranteed to behave correctly) if and only if the system has good particle order ( $\sum_b \epsilon_{ab} x_{ab}^n = 0$  if  $n$  is odd and  $= 1$  if  $n$  is even).

<sup>4</sup> This is directly analogous to the known behavior of the SPH momentum equation if the discretization uses the zeroth-order accurate derivative approximation in Eq. 20 (see Morris 1996; Abel 2011; Price 2012).

<sup>5</sup> We can also trivially take variants of Eq. 25 by replacing the  $\rho, \mathbf{K}, \nabla W$ , or  $\langle \nabla \otimes \mathbf{q} \rangle$  terms with symmetrized versions of themselves (e.g.  $\rho_{a,b} \rightarrow (\rho_a + \rho_b)/2$  or  $\sqrt{\rho_a \rho_b}$ ), but these have very small effects on the results.

mulation, first arrive at a slightly different version of Eq. 17, identical up to the replacement

$$\mathbf{K} \rightarrow \tilde{\mathbf{K}} \equiv \mathbf{K} - \mathbf{K}_{\text{corr}} \quad (28)$$

$$\mathbf{K}_{\text{corr}} \equiv \frac{1}{2} (\text{Trace}(\mathbf{K}) \mathbf{I} - N_{\text{Dim}} \mathbf{K}) \quad (29)$$

where  $N_{\text{Dim}}$  is the number of spatial directions in which the particles are locally distributed.

This equation minimizes the integral of the leading-order SPH errors in the continuum limit, for isotropically distributed particles in  $N_{\text{Dim}}$  dimensions. The term  $\mathbf{K}_{\text{corr}}$  accounts for the fact that, for isotropically distributed particles, there is a non-zero rms projection of the particle separation vectors onto  $\mathbf{K}$  – the resulting systematic error term is estimated from an integral formulation (in the continuum limit), and then subtracted.

However, as the authors themselves noted, this formulation is numerically unstable. This is easy to see for the simple case of scalar diffusion with  $\mathbf{K} = K \hat{\mathbf{B}} \otimes \hat{\mathbf{B}}$ , where the term  $\hat{\mathbf{x}}^T \mathbf{K} \hat{\mathbf{x}} \rightarrow |\hat{\mathbf{B}} \cdot \hat{\mathbf{x}}_{ij}|^2$  in our Eq. 17 becomes  $\hat{\mathbf{x}}^T \tilde{\mathbf{K}} \hat{\mathbf{x}} \rightarrow K (5 |\hat{\mathbf{B}} \cdot \hat{\mathbf{x}}_{ij}|^2 - 1)/2$  (in 3D). This becomes negative for  $|\hat{\mathbf{B}} \cdot \hat{\mathbf{x}}_{ij}| < 1/\sqrt{5}$ , i.e. the diffusivity becomes negative, and heat flows from cold to hot. We stress that this instability is much more severe compared to the instability encountered in the “gradients of gradients” method. Consider the case where a kernel (centered on a particle at  $\mathbf{x}_0$ ) is sufficiently poorly-sampled such that most particles in a kernel have  $|(\mathbf{x} - \mathbf{x}_0) \cdot \hat{\mathbf{B}}| \ll |\mathbf{x} - \mathbf{x}_0|$  (for example, if most of the particles lie close to a plane perpendicular to  $\hat{\mathbf{B}}$ ). Then *all* particles in the kernel meet the instability condition, and errors quickly dominate the entire domain. Even worse, if the problem involves, say, a thin sheet or disk with a perpendicular magnetic field (or *any* 2D problem with particles in the  $x - y$  plane and  $\hat{\mathbf{B}} = \hat{\mathbf{z}}$ ), then the diffusivity  $\hat{\mathbf{x}}^T \tilde{\mathbf{K}} \hat{\mathbf{x}} \rightarrow -K/2$  is *everywhere* negative.

There are two ways to restore stability in this method. First, we can add a numerical diffusion term  $\mathbf{K}_{\text{art}}$  to ensure  $\tilde{\mathbf{K}}$  is positive-definite (guaranteeing unconditional stability), i.e. take  $\tilde{\mathbf{K}} \rightarrow \tilde{\mathbf{K}} + \mathbf{K}_{\text{art}}$ . Petkova & Springel (2009) show that the minimum required numerical diffusivity is *exactly*  $\mathbf{K}_{\text{art}} = \mathbf{K}_{\text{corr}}$ , so  $\tilde{\mathbf{K}} \rightarrow \mathbf{K}$ . In other words, we simply obtain our “default” SPH prescription.

Alternatively, we can restore stability by adding a flux-limiter. The simplest would replace  $\hat{\mathbf{x}}^T \tilde{\mathbf{K}} \hat{\mathbf{x}} \rightarrow \text{MAX}(\hat{\mathbf{x}}^T \tilde{\mathbf{K}} \hat{\mathbf{x}}, 0)$ , but we have experimented with  $\sim 50$  different flux/slope-limiter combinations. We find the best results, again, using a similar flux-limiter to our MFM method, where we divide the numerical flux into a component in  $\tilde{\mathbf{K}}$  which forms our  $\mathbf{F}_2$  and a diffusive component in  $\mathbf{K}_{\text{art}}$  which forms  $\mathbf{F}_U$ . Unfortunately, with *any* of the flux-limiters we have explored, we are forced to (by definition) suppress the full “error subtraction” term  $\mathbf{K}_{\text{corr}}$ , and will show that this re-introduces the same systematic, non-convergent errors as our default approach.

### 3.3 An Improved Integral-Godunov SPH Formulation

The systematic error in SPH has deep roots. Consider a simple scalar diffusion problem, with perpendicular fields (perfect anisotropic suppression). In our default SPH (Eq. 17), or second-kernel-derivative SPH, or error-subtracted SPH, the diffusion equation can be written:

$$\frac{d(VU)_i}{dt} = \sum_j \varpi_{ij} (q_j - q_i) F(\mathbf{x}_{ij}, \mathbf{K}_{ij}) \quad (30)$$

where  $\varpi_{ij}$  is a positive-definite scalar weight factor, and  $F$  is some function of the particle separation  $\mathbf{x}_{ij} = \mathbf{x}_j - \mathbf{x}_i$  and diffusivity  $\mathbf{K}_{ij} = (\mathbf{K}_i + \mathbf{K}_j)/2$ . Numerical stability requires  $F$  is positive-definite, but it is *impossible* to construct a non-trivial positive-definite function

$F(\mathbf{x}_{ij}, \mathbf{K}_{ij})$  which vanishes in the perpendicular case for *arbitrary* particle configurations  $\mathbf{x}_{ij}$ , except when  $\mathbf{K}_{ij} = 0$  itself vanishes.

If we instead adopt the “gradients-of-gradients” approach, this generalizes to:

$$\frac{d(VU)_i}{dt} = \sum_j \varpi_{ij} (q_j - q_i) F(\mathbf{x}_{ij}, \mathbf{K}_{ij}, \langle \nabla q \rangle_{ij}) \quad (31)$$

Now, it is possible to construct a non-trivial positive-definite  $F$  which vanishes in the perpendicular case: for example any  $F \propto |\mathbf{K}_{ij} \cdot \langle \nabla q \rangle_{ij}|$ . Note that we must still invoke some flux-limiter to ensure  $F$  is positive-definite (since obviously  $F \propto \mathbf{K}_{ij} \cdot \langle \nabla q \rangle_{ij}$  can change sign), but can be done in the manner of our MFM method.

However, as shown in § 3.2.2, this will only *correctly* determine the gradients and so return a vanishing  $F$  if the gradient operator  $\langle \nabla q \rangle_{ij}$  is at least second-order accurate (in both the gradient magnitude and direction, independent of the local particle arrangement). This is not true of the standard SPH operator. But there are gradient operators which satisfy this – for example, the moving least-squares estimator adopted for our MFM method.

Therefore, our “improved” SPH formulation involves the following steps. We begin with the “gradients-of-gradients” method described in § 3.2.2, and Eq. 25. Then:

(1): Replace the standard SPH gradient estimator (Eqs. 20 & 24) with our second-order accurate moving-least squares estimator from our MFM method (Eq. 4), to define  $\langle \nabla \otimes \mathbf{q} \rangle$ .

(2): The particular form of Eq. 25 is difficult to stabilize, and has a systematic inaccuracy at contact discontinuities. These can be remedied by symmetrizing the density terms and smoothing length terms as they appear, resulting instead in the modified equation:

$$\frac{d(VU)_a^{\text{SPH}}}{dt} = - \sum_b \mathbf{A}_{ab}^{\text{SPH}} \cdot \mathbf{F}_{\text{diff}}^{\text{SPH}} \quad (32)$$

$$\mathbf{A}_{ab}^{\text{SPH}} \equiv \frac{m_a m_b}{\rho_a \rho_b} (\nabla_a W_{ab} + \nabla_b W_{ab}) = V_a V_b \bar{\nabla} W_{ab} \quad (33)$$

$$\mathbf{F}_{\text{diff}}^{\text{SPH}} = -\frac{1}{2} (\mathbf{K}_a \cdot \langle \nabla \otimes \mathbf{q} \rangle_a + \mathbf{K}_b \cdot \langle \nabla \otimes \mathbf{q} \rangle_b) \quad (34)$$

(3): Stabilize the solution by replacing  $F_{\text{diff}}^{\text{SPH}}$  with  $F_{\text{diff}}^*$ , obtained by adding the appropriate numerical flux from solving a Riemann problem between the particles and flux-limiting the solution. We follow exactly our MFM procedure in § 2.2. We simply identify  $\mathbf{F}_{\text{diff},R} = \mathbf{K}_b \langle \nabla \otimes \mathbf{q} \rangle_b$  (and likewise  $L$  and  $a$ ).

Of course, with these fixes, there is almost nothing “SPH” about the method anymore! In fact, this method is now *exactly* identical to our finite-volume MFM and MFV methods, except that we replace the MFM/MFV faces  $\mathbf{A}_{ij}$  with an “effective SPH face,”  $\mathbf{A}_{ij}^{\text{SPH}}$  (Eq. 33). Hence we refer to this as “integral-Godunov SPH”: the “Godunov” because we now rely on fluxes through faces, determined by solution to a Riemann problem, and the “integral” because the derivative is estimated according to the matrix-integral formulation used to derive our MFM/MFV methods (see Lanson & Vila 2008a).

### 3.4 Timestepping

Timestepping requirements are identical in SPH and our MFM/MFV methods.

## 4 EXAMPLES IMPLEMENTED

We implement these methods in the code GIZMO. A number of specific physical cases have been implemented; our focus here is not on the microphysics but on the numerical methods. Still, it is useful to list the relevant examples, both to explicitly see how they

correspond to the general formulation above, and to give examples of the different forms of anisotropy that are physically expected.

#### 4.0.1 Isotropic Passive-Scalar Diffusion

For this simple case, we have

$$\mathbf{K} = \kappa \mathbf{I} \quad (35)$$

$$\mathbf{q} = \mathbf{U} = n_{\text{scalar}} \quad (36)$$

where  $\kappa$  is the (arbitrary) diffusion coefficient,  $\mathbf{I}$  the identity matrix, and  $n_{\text{scalar}}$  the scalar density.

#### 4.0.2 Anisotropic Thermal Conduction

Isotropic and anisotropic thermal conduction are represented by:

$$\mathbf{K} = \kappa_{\perp} \mathbf{I} + \kappa_{\parallel} \hat{\mathbf{B}} \otimes \hat{\mathbf{B}} \quad (37)$$

$$\mathbf{q} = T \mathbf{v}, \quad \mathbf{U} = \rho u \quad (38)$$

where  $T$  is the gas temperature,  $\rho$  the gas density and  $u$  the internal energy per unit mass,  $\kappa_{\perp}$  the isotropic diffusion coefficient,  $\kappa_{\parallel}$  the anisotropic (parallel) diffusion coefficient, and  $\hat{\mathbf{B}} \equiv \mathbf{B}/|\mathbf{B}|$  the direction of the local magnetic field. Here we allow either arbitrarily specified  $\kappa$ , or default to the Spitzer conductivity (for  $\kappa_{\parallel}$ , with  $\kappa_{\perp} = 0$ ) with a limiter for cases where the implied heat transport rate exceeds the free electron streaming rate.

#### 4.0.3 Anisotropic Cosmic Ray Diffusion & Streaming

Cosmic rays diffuse along magnetic field lines. Moreover, as shown by Uhlig et al. (2012), cosmic-ray streaming can be represented numerically via a diffusion operator. Therefore we have, for the simple case of a single-species cosmic-ray population

$$\mathbf{K} = (\kappa_{\text{diff}} + \kappa_{\text{stream}}) \hat{\mathbf{B}} \otimes \hat{\mathbf{B}} \quad (39)$$

$$\mathbf{q} = P_{\text{cr}} \mathbf{v}, \quad \mathbf{U} = e_{\text{cr}} \quad (40)$$

where  $P_{\text{cr}}$  is the cosmic ray pressure (proportional for a single-species model to the CR number density),  $e_{\text{cr}} \approx P_{\text{cr}}/(\gamma_{\text{cr}} - 1) = \rho u_{\text{cr}}$  is the cosmic ray energy density, and  $\kappa_{\text{diff}}$  and  $\kappa_{\text{stream}}$  are the appropriate “effective” coefficients for diffusion and streaming processes, respectively.

#### 4.0.4 Turbulent Eddy Diffusion Models

In popular “sub-grid” models for turbulence, the effect of unresolved eddies is treated as a diffusion process. Following the Smagorinsky (1963) model, we model this for e.g. diffusion of a scalar field via

$$\mathbf{K} = \rho (C \Delta x)^2 \|\mathbf{S}\| \mathbf{I} \quad (41)$$

$$\mathbf{q} = u_{\text{scalar}} \mathbf{v} = \frac{n_{\text{scalar}}}{\rho} \mathbf{v}, \quad \mathbf{U} = n_{\text{scalar}} \quad (42)$$

where  $\Delta x$  is the resolution scale (for our meshless methods, defined to be equal to the rms inter-element spacing inside the kernel),  $C \sim 0.1$  is a constant calibrated to numerical simulations in Smagorinsky (1963), and  $\mathbf{S}$  is the symmetric shear tensor.

#### 4.0.5 Anisotropic Radiation Transport in the Diffusion Limit

In the optically thick limit, the radiative transfer moment equations are commonly expressed as a diffusion equation. It is convenient to represent this in the form

$$\mathbf{F}_{\text{diff}} = -\mathbf{K} \cdot (\nabla \cdot \mathbf{q}) \quad (43)$$

$$\mathbf{K} = \frac{\lambda c}{\kappa_{\nu} \rho} \mathbf{I} \quad (44)$$

$$\mathbf{q} = n_{\nu} \mathbb{D}_{\nu} \mathbf{v}, \quad \mathbf{U} = n_{\nu} \quad (45)$$

where  $c$  is the speed of light,  $\kappa_{\nu}$  the opacity at frequency  $\nu$ ,  $n_{\nu}$  the photon number (or energy) density,  $\lambda$  an optional “radiative flux limiter,” and  $\mathbb{D}_{\nu}$  the dimensionless Eddington tensor. Note the  $\nabla \cdot \mathbf{q}$  instead of  $\nabla \otimes \mathbf{q}$  has no effect on our methodology, it simply re-orders the gradient terms in  $\mathbf{F}_{\text{diff}}$ . Various numerical methods (e.g. flux-limited diffusion and “variable Eddington tensor” methods) rely on this description.

#### 4.0.6 Anisotropic Viscosity

For a viscous fluid, we have

$$\mathbf{q} = \mathbf{v}, \quad \mathbf{U} = \rho \mathbf{v} \quad (46)$$

where  $\mathbf{v}$  is the velocity and  $\rho$  the density. In this case the form of  $\mathbf{F}_{\text{diff}}$  depends on the viscous parameterization. In the case of a magnetized fluid, the Braginskii viscosity can be written

$$\mathbf{F}_{\text{diff}} = -\mathbf{K} \left[ \hat{\mathbf{K}} : (\nabla \otimes \mathbf{q}) \right] \quad (47)$$

$$\mathbf{K} = 3\nu_{\parallel} \left( \hat{\mathbf{B}} \otimes \hat{\mathbf{B}} - \frac{1}{3} \mathbf{I} \right) \quad (48)$$

$$\hat{\mathbf{K}} = \frac{\mathbf{K}}{3\nu_{\parallel}} = \hat{\mathbf{B}} \otimes \hat{\mathbf{B}} - \frac{1}{3} \mathbf{I} \quad (49)$$

while for the un-magnetized case, it is common practice to decompose the viscosity into shear ( $\eta$ ) and bulk ( $\zeta$ ) terms, following

$$\mathbf{F}_{\text{diff}} = \Pi_{\eta} + \Pi_{\zeta} \quad (50)$$

$$\Pi_{\eta} = -\mathbf{K}_{\eta} \left[ \nabla \otimes \mathbf{q} + (\nabla \otimes \mathbf{q})^T - \frac{2}{3} (\nabla \cdot \mathbf{q}) \mathbf{I} \right], \quad \mathbf{K}_{\eta} = \eta \mathbf{I} \quad (51)$$

$$\Pi_{\zeta} = -\mathbf{K}_{\zeta} (\nabla \cdot \mathbf{q}), \quad \mathbf{K}_{\zeta} = \zeta \mathbf{I} \quad (52)$$

Here “:” denotes the double-dot-product. As above, the particular arrangement of  $\mathbf{K}$  and  $\hat{\mathbf{K}}$  within the double-dot-product (for the magnetized case) or decomposition of  $\nabla \otimes \mathbf{v}$  into shear/bulk terms have no effect on our methodology; they simply re-order the gradients of  $\mathbf{q}$  within  $\mathbf{F}_{\text{diff}}$ . As with conduction we allow either freely-specified  $\eta$ ,  $\zeta$ ,  $\nu_{\parallel}$ , or can calculate the coefficients according to Spitzer-Braginskii theory with the appropriate limiters. We also add the corresponding viscous term to the energy equation.

#### 4.0.7 Non-Ideal MHD

Astrophysical non-ideal MHD effects are typically parameterized as Ohmic dissipation (controlled by the resistivity  $\eta_0$ ), the Hall effect ( $\eta_H$ ) and ambipolar diffusion ( $\eta_A$ ). All appear as diffusion operators in the induction equation; if we operator-split the ideal MHD term (already solved in GIZMO), we have

$$\frac{d\mathbf{B}}{dt} = -\nabla \times [\eta_0 \mathbf{J} + \eta_H (\mathbf{J} \times \hat{\mathbf{B}}) - \eta_A (\mathbf{J} \times \hat{\mathbf{B}}) \times \hat{\mathbf{B}}] \quad (53)$$

where  $\mathbf{J} = \nabla \times \mathbf{B}$ . We can, with some elaborate algebra, write this as an equation in  $\nabla \cdot \mathbf{F}_{\text{diff}}$ , but it is easier to cast this directly into the alternative Godunov form:

$$\frac{d}{dt} (V \mathbf{U})_i = - \sum_j \mathbf{A}_{ij} \times \mathbf{F}_{\text{diff},ij}^* \quad (54)$$

$$\mathbf{F}_{\text{diff}} = -[\mathbf{K}_O + \mathbf{K}_H + \mathbf{K}_A] \cdot (\nabla \times \mathbf{q}) = -\mathbf{K} \cdot (\nabla \times \mathbf{q}) \quad (55)$$

$$\mathbf{K}_O = \eta_0 \mathbf{I} \quad (56)$$

$$\mathbf{K}_A = \eta_A (\mathbf{I} - \hat{\mathbf{B}} \otimes \hat{\mathbf{B}}) \quad (57)$$

$$\mathbf{K}_H = \eta_H \begin{bmatrix} 0 & \hat{B}_z & -\hat{B}_y \\ -\hat{B}_z & 0 & \hat{B}_x \\ \hat{B}_y & -\hat{B}_x & 0 \end{bmatrix} \quad (58)$$

$$\mathbf{q} = \mathbf{B}, \quad \mathbf{U} = \mathbf{B} \quad (59)$$

where  $\hat{B}_x, \hat{B}_y, \hat{B}_z$  are the components of  $\hat{\mathbf{B}}$  and the coefficients are calculated from the plasma properties. The appropriate magnetic terms are added to the energy equation.

## 5 NUMERICAL TESTS

### 5.1 Diffusing Sheet

For a first test, we study a simple discontinuity in one dimension,  $\mathbf{q} = \mathbf{q}_L$  for  $x < 0$ ,  $\mathbf{q} = \mathbf{q}_R$  for  $x > 0$ , with all other properties fixed. To focus on the diffusion equations, we turn off all MHD forces (for now). We also simulate this in a 3D box, because although it is essentially a 1D problem, sensitivity to particle arrangement makes accurate solution much more challenging in 2D or 3D. Finally, we also add noise (which is critical to test for numerical instability): we add a uniform random value to  $q$  between  $\pm 0.05 q_L$ , for all particles.

#### 5.1.1 Isotropic Case

In the isotropic case, after the noise has been (quickly) damped away,<sup>8</sup> this has the trivial analytic solution

$$q(x, t) = \frac{q_R + q_L}{2} + \frac{q_R - q_L}{2} \operatorname{Erf} \left[ \frac{x}{\sqrt{4\kappa t}} \right] \quad (60)$$

The solution is completely self-similar so the absolute values of all quantities are irrelevant; the only numerically important quantity is the number of resolution elements over which the contact discontinuity has been diffused  $\sim \sqrt{4\kappa t}/\Delta x$  (as we evolve the solution, it becomes better-resolved). We therefore plot results at fixed  $\sqrt{4\kappa t}/\langle \Delta x \rangle$ .

Our results converge well to the analytic solution with both methods even at low resolution ( $\sqrt{4\kappa t}/\langle \Delta x \rangle \gtrsim 4$ ). Because the initial noise is grid-scale, it should be damped away on a small timescale  $\sqrt{4\kappa t}/\langle \Delta x \rangle \sim 1$ ; we confirm this.

Note that the solution here is independent of the physics; we have explicitly verified that our implementations of passive-scalar diffusion ( $n \propto q(x, t)$  above), conduction ( $T \propto q$  with  $\mathbf{K} = \kappa_{\perp} \mathbf{I}$ ), cosmic rays ( $e_{\text{cr}} \propto q$ , with  $\mathbf{K} = \kappa_{\text{diff}} \mathbf{I}$ ), eddy diffusion ( $n \propto q$ ), isotropic radiation transport ( $n_{\nu} \propto q$  with  $\mathbb{D}_{\nu} = \mathbf{I}/3$ ), viscosity ( $\mathbf{B} = 0$  with  $v_x = v_z = 0$ ,  $v_y \propto q$ , and  $\zeta = 0$ ), and Ohmic resistivity ( $B_y \propto q$ ) all give *identical* results on this test (given the same diffusivity), as they should.

#### 5.1.2 Anisotropic Case

Next we consider the anisotropic case. Here we take  $\mathbf{K} = \kappa \hat{\mathbf{B}} \otimes \hat{\mathbf{B}}$  with  $\kappa$  and  $\hat{\mathbf{B}}$  constant and  $|\hat{\mathbf{B}}| = 1$ . In this case, the solution is identical to the isotropic case but with  $\kappa \rightarrow \kappa |\hat{\mathbf{B}} \cdot \hat{\mathbf{x}}|^2 = \kappa \hat{B}_x^2$ , so it is entirely specified by the absolute value of the projection of  $\hat{\mathbf{B}}$  in the gradient ( $\hat{\mathbf{x}}$ ) direction,  $|\hat{B}_x|$ .

We have considered  $\sim 100$  values between  $-1 \leq \hat{B}_x \leq 1$  to check for pathological behavior; these are summarized with three representative cases shown here:  $|\hat{B}_x| = 0$  (perpendicular fields, which should completely suppress diffusion),  $|\hat{B}_x| = 1$  (parallel fields; the solution should be identical to the isotropic case), and  $|\hat{B}_x| = 1/\sqrt{2}$ .

For all scalar diffusion cases (passive scalars, cosmic rays, eddy diffusion, conduction) this gives identical results. For our radiation diffusion, we make the system anisotropic by instead taking

$\mathbb{D} = \hat{n} \otimes \hat{n}$ , with  $\hat{n} = \hat{\mathbf{B}}$  constant. For this problem, this should produce exactly identical solutions to our cases above, and we confirm this for both SPH and MFM.

Our MFM method is able to handle all three cases accurately; we confirm that there is zero diffusivity for the perpendicular case (up to machine precision, if our initial  $\mathbf{q}$  depends on  $x$  alone) and that the parallel case exactly matches the isotropic case. Convergence is again good even at low resolution  $\sqrt{4\kappa t}/\Delta x \gtrsim 4$ , and (we show below) the results are insensitive to noise or particle order.

In our “standard” SPH formulation (§ 3.1), significant systematic errors appear in both parallel and perpendicular cases. In the parallel case the diffusivity is systematically suppressed by  $\sim 30\%$  relative to the correct solution. In the perpendicular case we do not see complete suppression, but rather about  $\sim 1/5$  of the isotropic diffusivity (i.e. the equivalent of  $\hat{B}_x = 1/\sqrt{5}$ ). This leads to qualitatively incorrect behavior. Note that both behaviors apply at all times (we can run the problem arbitrarily long times, and the error does not decrease), and at all resolutions and particle neighbor numbers (shown below). This owes to the systematic errors discussed in § 3.1.2: the fact that gradients are assumed to lie, locally, *along inter-particle separation vectors* means that there is will always be some neighbors with non-vanishing projection of the gradient onto  $\hat{\mathbf{B}}$ , regardless of the orientation of  $\hat{\mathbf{B}}$  (similarly, there will always be neighbors with less-than-perfect projection, in the parallel case). This means neither completely parallel nor completely perpendicular cases can be captured with this SPH formulation.<sup>9</sup> These results are in excellent agreement similar tests performed in Arth et al. (2014) for anisotropic conduction; we have also verified that we reproduce all the tests in Petkova & Springel (2009) for the radiation case (Khatami et al., in preparation).

However, our “improved” integral-Godunov SPH method from § 3.3, which is essentially identical to our finite-volume MFM and MFV methods but with a different definition of the “effective faces” between particles, agrees very well with our MFM results.

#### 5.1.3 Dependence on Particle Order, Resolution, Noise, and Neighbor Number

Fig. 2 considers variations of the anisotropic sheet.

In order to test whether our methods are sensitive to the local arrangement of particles, we have considered (in both 2D and 3D tests) an initial particle distribution following (1) a regular square lattice, (2) uniformly randomly-distributed particles over the volume (a Poisson distribution), (3) a glass (generated from the random distribution), and (4) a densest sphere packing. In 2D we have also considered a regular triangular and hexagonal grid. For our MFM/MFV method, the results are almost indistinguishable (after the initial noise is damped) in every one of these cases (even the “worst-case” Poisson distribution, shown in Fig. 2), clearly demonstrating that the method does not depend sensitively on particle order. In SPH, there is a weak dependence on the exact particle configuration – as one might expect, the disordered (Poisson) configuration produces more noise.

We consider resolution tests, varying both the absolute resolution and number of kernel neighbors. Our MFM/MFV and improved integral-Godunov SPH results are well-converged even with just  $\sim 4 - 8$  resolution elements across the jump (i.e.

<sup>8</sup> We have considered both a perfect step-function initial condition, and (alternatively) initializing the profile with the analytic solution corresponding to time  $t_0$  such that  $\sqrt{4\kappa t_0}/\langle \Delta x \rangle \approx 2$ . These are indistinguishable after a short time ( $\sqrt{4\kappa t_0}/\langle \Delta x \rangle \gtrsim 4$ ).

<sup>9</sup> Interestingly, in the “standard” SPH formulation, the  $\hat{B}_x = 1/\sqrt{2}$  case is captured almost perfectly – this corresponds to the case where the systematic errors cancel, given the specific initial particle arrangement here.

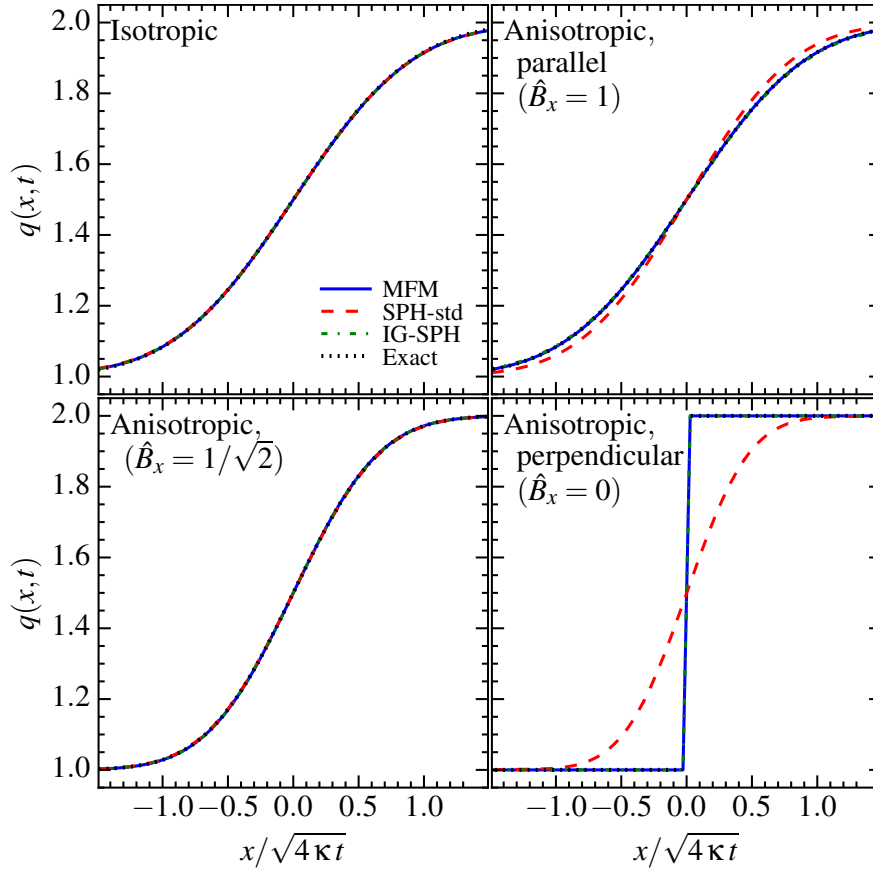


**Figure 1.** Diffusing sheet test (§ 5.1). A 3D box ( $N = 64$  elements across plotted  $x$ -range) is initialized with a step-function discontinuity ( $x = 0$ ) in diffusing quantity  $\mathbf{q}$ . The solution is scale-free in units shown, and independent of the physics (we confirm identical behavior for implementations of passive-scale diffusion, conduction, radiation transport in the diffusion limit, viscosity, and Ohmic resistivity; § 4). We consider isotropic and anisotropic cases with diffusion tensor  $\mathbf{K} = K(\hat{\mathbf{B}} \otimes \hat{\mathbf{B}})$ , with parallel, partially-aligned, and perpendicular fields  $\mathbf{B}$ . In each case we compare our mesh-free finite-element methods (MFM, our MFV method is manifestly identical on these problems; § 2); the most accurate of the numerically stable “standard” SPH formulations (SPH-std; § 3.1); and our new integral-Godunov SPH (IG-SPH; § 3.3). Our MFM/MFV and IG-SPH methods recover the exact solutions accurately. Standard SPH does well in isotropic cases but systematically over (under) predicts the diffusivity in perpendicular (parallel) cases.

( $\sqrt{4\kappa t}/\Delta x \gtrsim 4$ ). The convergence rate of our MFM/MFV methods is also independent of neighbor number, as shown in Paper I and Paper II (going to larger neighbor number simply trades a reduction in noise for increased numerical diffusivity).

Most troublingly, the “standard” SPH systematic errors do not converge with resolution, *nor* with increasing neighbor number. This is because, as noted above and shown rigorously in Petkova & Springel (2009), there is, even assuming an isotropic configuration of particles, a non-vanishing systematic error term owing to the rms projection of particles on the gradient direction even in the fully-suppressed case.

We have also tested for sensitivity to initial noise, varying the seed noise level from 0 – 25% of the jump level. In all cases our results are stable and do not qualitatively change with respect to this. Likewise, the steepness of the initial discontinuity has no effect on our results (whether we begin with the full solution at a resolved scale, or a perfectly steep discontinuity across a single particle).

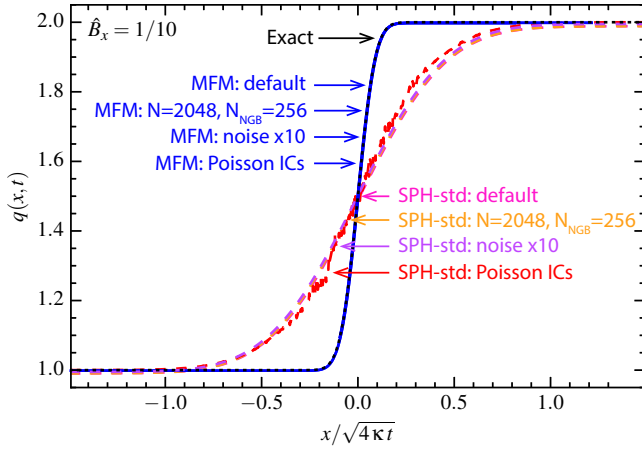
#### 5.1.4 Results in Alternative SPH Formulations

Fig. 3 compares the alternative SPH operators from § 3.2, with and without limiters included to numerically stabilize their fluxes, in the diffusing sheet. In the case without limiters, we consider simulations with the same anisotropy (same  $\mathbf{K} = K\hat{\mathbf{B}} \otimes \hat{\mathbf{B}}$ ) but two different initial conditions: first a “perfect” IC, with zero noise and particles in an ideal lattice (which can mask the presence of insta-

bility, since there is no seed noise to amplify), and second a “perturbed” IC with  $\sim 2\%$  initial noise seeded randomly in  $\mathbf{q}$  and the particle positions perturbed by  $\sim 10\%$  from their ideal lattice positions before the quantities are initialized (this represents a much more realistic scenario for typical problems). Fig. 3 also shows the results if we add slope and/or flux limiters to stabilize the methods – in each case we show results for the limiter, of the  $\sim 50$  we have experimented with, which gives the best performance on this test (generally close to the form in our MFM method). In these cases we consider both perpendicular and parallel-field simulations.

First consider the second-kernel-derivative SPH formulation. As expected this is completely noise-dominated. Without limiters the instability is catastrophic and the code eventually crashes, regardless of the noise level and particle order in the ICs. With limiters the code runs but with severe noise; note that we were forced to use  $\sim 128$  neighbors in a quartic spline in the version shown, instead of our usual  $\sim 32$ , just to obtain a solution which was visible on the plot. Even going to  $\sim 500$  neighbors in the kernel, we find this gives noisier results than the standard SPH with  $\sim 32$  neighbors, and does not eliminate the systematic errors of the standard SPH method.

The “gradients of gradients” SPH method (using the standard SPH gradient estimator) also requires limiters be added, or else the



**Figure 2.** Anisotropic sheet (as Fig. 1) with varied ICs (§ 5.1.3). We compare (1) A “default” case with resolution  $N = 64$  particles across the plotted range in the  $x$ -direction ( $\approx 4$  particles across the range of diffusion at this time, in MFM), and effective neighbor number  $N_{\text{NGB}} = 32$  within the kernel partition function. Particles are initially in a cubic lattice, with noise in  $\mathbf{q}$  equal to 2.5% of the jump value. (2) High-resolution ( $N = 2048$ ) and neighbor number ( $N_{\text{NGB}} = 256$ , with a quintic kernel function). (3) Initial noise = 25% of jump value. (4) Initial particles laid down randomly (according to a Poisson distribution). Our MFM results are indistinguishable from each other and the exact solution in each case. IG-SPH (not shown) is nearly identical to MFM here. Standard SPH is insensitive to the initial noise in  $\mathbf{q}$ , but sensitive to the particle configuration, and its systematic errors are independent of resolution and neighbor number.

numerical instability can destroy the solution.<sup>10</sup> The instability is slightly worse if we begin from noisy ICs or ICs without perfect particle order, but is actually comparable even with perfect ICs. Interestingly, if we consider the “perfect ICs” case *and* begin the simulation from a second-order smooth, resolved gradient (as opposed to a discontinuity), or consider the case with exactly perpendicular fields (no diffusion), then we obtain good solutions. This is because, as shown in Wurster et al. (2014), in this particular limit various errors vanish and the (un-limited) gradient-of-gradient method becomes both consistent and stable. With appropriate limiters, this method is unconditionally stable, and (owing to the explicit presence of a  $\mathbf{K} \cdot \langle \nabla \otimes \mathbf{q} \rangle$  term) is able to better capture the fully-suppressed (perpendicular) case compared to standard SPH (the maximum suppression factor is  $\sim 15$ ). However, the diffusion in the parallel case is still under-estimated systematically (and this error does not converge with resolution), and in both cases the noise is substantially larger than our “standard” SPH method.

In the “error-corrected” formulation, the unstable formulation might at first appear to better treat anisotropic cases if we only consider “perfect” ICs. However there are three problems. First, the addition of a small amount of noise or particle disorder (e.g. our “perturbed” IC) can violently de-stabilize the method. Second, certain geometric configurations simply cannot be handled: if we simulate a thin sheet (particles in  $x-y$  plane) with perpendicular  $\mathbf{B} \propto \hat{z}$ , “error-corrected” SPH has everywhere negative conductivity and fails catastrophically (even with perfect ICs). Third, even the perfect-IC case shown clearly exhibits numerical insta-

<sup>10</sup> Note, we do not include any of the usual SPH “artificial dissipation” terms in this test because we want to study the diffusion equation alone. Those are sufficient to prevent numerical instability from severely corrupting the domain in this test; however, that only means the incorrect physical terms are being re-distributed by other forces.

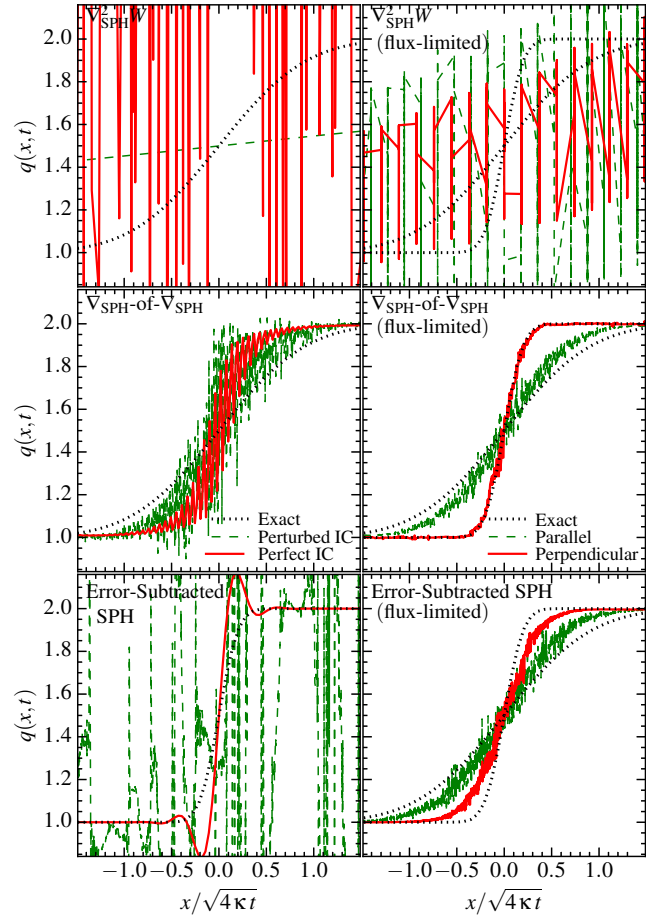


**Figure 3.** Diffusing sheet (as Fig. 1) in alternative “standard” SPH formulations § 3.2. *Left:* Without explicit flux-limiters: these methods are all numerically unstable. We show a single anisotropic case and compare a “perfect initial condition” (IC) with no noise and perfect particle lattice order, and one with  $\sim 2\%$  initial noise in  $\mathbf{q}$  and particle positions perturbed by  $\sim 10\%$  of the inter-particle separation. *Right:* Same, but with the most accurate flux-limiters of those we study. We compare parallel ( $\hat{B}_x = 1$ ) and perpendicular ( $\hat{B}_x = 0$ ) cases, with “perturbed” ICs. *Top:* Second derivatives estimated directly from second-kernel derivatives (§ 3.2.1). The noise in this estimator is catastrophic even with  $\gg 100$  neighbor particles in the kernel and flux-limiters. *Middle:* Second derivatives estimated from successive applications of the SPH first-derivative operator (§ 3.2.2). This produces the same systematic errors as our “standard” SPH method in the parallel case (though suppression is improved in the perpendicular case), with increased noise. *Bottom:* The “standard” integral formulation, but attempting to subtract the systematic error term (§ 3.2.3). Even without a flux-limiter, a systematic error still exists in the perpendicular case but with reversed sign (negative diffusivity creates the “peaks”). With flux-limiters the systematic errors are comparable to our “standard SPH” method and noise is increased. In all cases here, even with the perfect ICs, numerical instability is clearly evident if we remove flux-limiters and produces noisy and systematically incorrect solutions; with small perturbations the errors are catastrophic.

bility in the “spikes” around the discontinuity, which result from systematically negative diffusivity, and this error *does not* converge away. In fact, all cases with  $|\hat{B} \cdot \hat{x}| \ll 1$  exhibit systematic negative diffusivity: we have simply replaced our previous systematic errors with new, smaller but un-physical (sign-swapped) systematic errors. This is again consistent with the results found in the papers where this method was derived (see Petkova & Springel 2009; Arth et al. 2014). Stabilizing the “error-corrected” SPH method by adding a numerical diffusivity simply returns our “standard” SPH method. We can stabilize instead with flux limiters, as shown, but

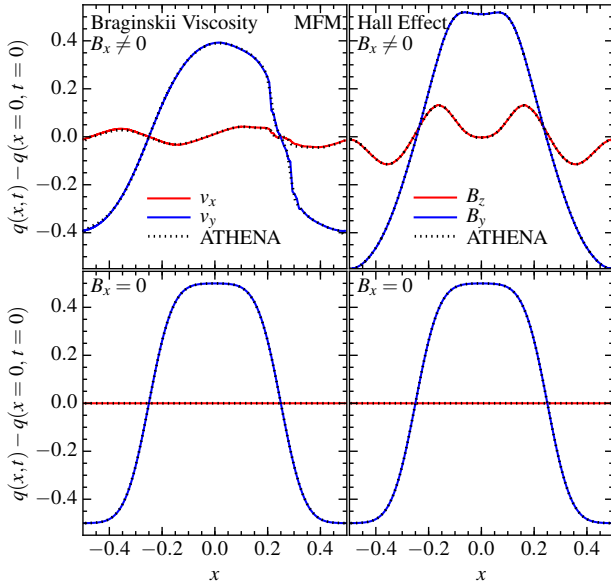


**Figure 4.** Anisotropic diffusing sheet problem, as Fig. 1 ( $N = 64$ ), but here focusing on two special cases where the solution is not the same as in Fig. 1 (see § 5.1.5). We consider MFMM here, and SPH in Fig. 5 below. There is no analytic solution for the cases shown, so, we compare a converged solution from ATHENA. *Left:* Braginskii viscosity (§ 4.0.6). The initial discontinuity is in  $v_y$  only, but this form of viscosity generates  $v_x \neq 0$  at later times. We consider two cases:  $\hat{B} = (1, 1, 0)/\sqrt{2}$  (*upper*; this should produce non-zero diffusion) and  $\hat{B} = (0, 1, 0)$  (*lower*; this should have vanishing diffusion). *Right:* Hall effect (§ 4.0.7). The initial discontinuity is in  $B_y$  ( $B_x = \text{constant}$ ,  $B_z$  vanishes). We consider a case which should diffuse ( $B_x \neq 0$ ; *upper*) and one which should be suppressed ( $B_x = 0$ ; *lower*). MFMM and ATHENA agree well in all cases.

this leads to the same systematic errors as our standard SPH (and larger noise).

We conclude that no “standard” formulation of anisotropic diffusion in SPH (of those we are aware of) is able to avoid serious systematic errors that do not converge (or worse yet, numerical instability). Our IG-SPH method therefore represents a major improvement over these formulations.

### 5.1.5 Braginskii Viscosity and the Hall Effect

Two of the physical cases in § 4 are more complicated, even in the simple diffusing sheet setup. These are Braginskii viscosity (§ 4.0.6) and the Hall effect (§ 4.0.7). In both,  $\mathbf{q}$  is a vector ( $\mathbf{v}$  or  $\mathbf{B}$ , respectively), and even if we initialize a gradient only in one element of that vector and set the other elements to vanish everywhere, the form of the diffusion operator leads to growth of other components of  $\mathbf{q}$ . Mathematically, the anisotropic part of the diffusion operator in most cases is a projection operator; here, it also includes a rotation operator. This leads to different non-linear solutions and makes it more challenging to achieve stable, accurate results.

Therefore we consider these cases specifically in Figs. 4-5. Since the non-linear solutions do not have analytic forms even for this simple test, we compare to a converged, high-resolution ( $N = 2048$  across the plotted domain), one-dimensional solution from the well-tested grid-based code ATHENA (Stone et al. 2008). We run ATHENA in its most accurate constrained-transport, PPM-CTU (highest-order) mode. For simplicity, we do not disable the other hydrodynamic forces, but these are not dominant. To avoid certain boundary condition effects in ATHENA we initialize the test

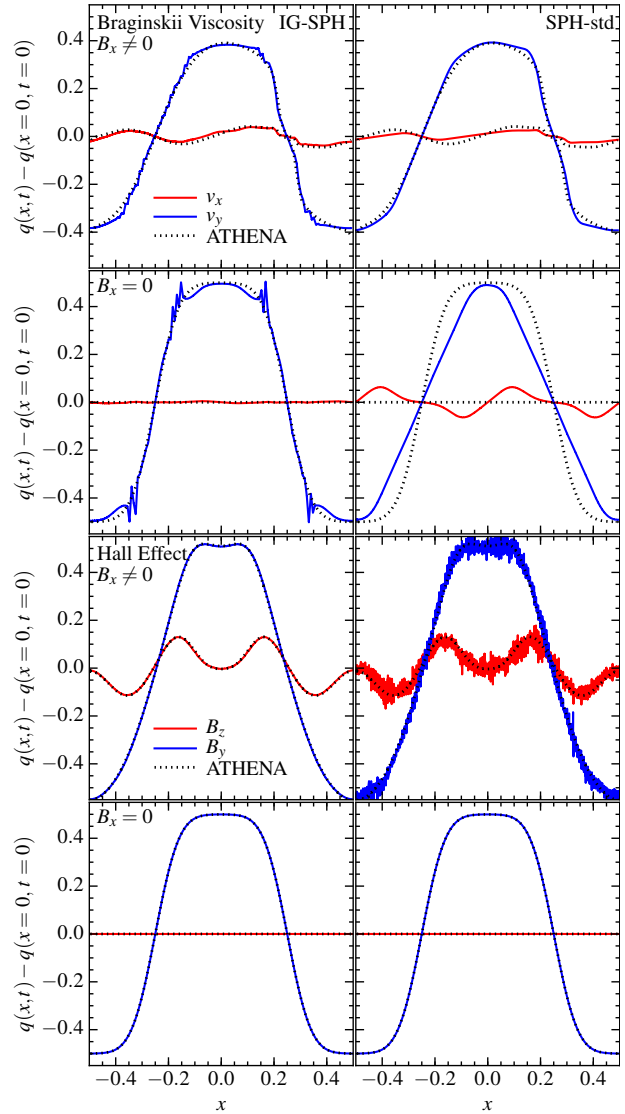


**Figure 5.** Braginskii viscosity (*top*) and the Hall effect (*bottom*), as Fig. 4, but comparing both our improved IG-SPH (*left*) and standard SPH (*right*) methods. In the Braginskii viscosity case, both SPH versions capture the major features for the diffusing ( $B_x \neq 0$ ) case, but disagree in detail with ATHENA. Standard SPH shows a failure to suppress diffusion in the fully-suppressed ( $B_x = 0$ ) case; IG-SPH performs better but shows substantial noise around the shear layers. The errors in IG-SPH owe to (1) the presence of SPH artificial viscosity, which tends to smear certain types of velocity structures and generates some spurious resolution-scale structure, and (2) a residual zeroth-order error in the orientations of the SPH “effective faces.” Both SPH methods can capture complete suppression for the Hall effect; in the diffusing ( $B_x \neq 0$ ) case, standard SPH produces serious noise owing to errors in the gradient estimator and SPH divergence-cleaning, but these are resolved in IG-SPH.

problem in slightly different fashion: we take

$$q = 1.5 - 0.5 \left( 1 + \text{Erf} \left[ \frac{x - 0.25}{0.01} \right] - \text{Erf} \left[ \frac{x + 0.25}{0.01} \right] \right) \quad (61)$$

For the Braginskii problem, we take initial  $\mathbf{v} = (0, q, 0)$  and consider both  $\hat{B} = (1, 0, 0)$  (which should produce zero diffusion) and  $\hat{B} = (1, 1, 0)/\sqrt{2}$  (which should diffuse); we take  $\rho = u = 1$ , and  $|\mathbf{B}| = 10^{-6}$  to be small so it has no effect on the dynamics except to control the anisotropy. For the Hall problem, we take vanishing initial velocities and  $\mathbf{B} = 10^{-6} (0, q, 0)$  (no diffusion)  $\mathbf{B} = 10^{-6} (1, q, 0)$  (diffusion).

Figs. 4-5 show these develop non-zero  $v_x$  and  $B_z$ , despite these vector components initially vanishing. In both cases our MFM/MFV methods produce solutions in excellent agreement with ATHENA, even well into non-linear evolution. Both cases with diffusion, and cases with full anisotropic suppression, are captured.

In the Braginskii problem, for the case with non-vanishing diffusion ( $\hat{B} = (1, 1, 0)/\sqrt{2}$ ), standard SPH produces the basic features, but disagrees in detail. Some features are over-smoothed, others remain too sharp. For the case where there should be no diffusion, SPH fails to capture the suppression: the “effective” diffusivity is very crudely  $\sim 1/4$  of the previous case, but we stress that the non-linear solution in this case is *not* simply the solution for a different diffusivity (it does not correspond to a real physical case, but is dominated by the systematic gradient errors). These errors do not converge with resolution. IG-SPH does not completely remedy the SPH errors. The case with non-vanishing diffusion shows similar (albeit different in detail) errors to SPH-std; the case with vanishing diffusion shows much better, but not complete, suppression, and some substantial noise at the edges of the discontinuity in  $v_y$ . These errors are driven by two effects. First, the SPH artificial viscosity (present in both SPH-std and IG-SPH) – here we use the “inviscid SPH” formulation from Cullen & Dehnen (2010) (for details see Paper I); however this still produces significant excess viscosity beyond the Riemann solver used in ATHENA and MFM/MFV, at certain points in the domain. Second, the effective face in IG-SPH is distinct from that in MFM. As discussed above, while IG-SPH is similar to MFM, the faces in all SPH methods are still assumed to be oriented always along the lines connecting particles. When the particle distribution is anisotropic (as it always will be at some times, when the particles are shearing), this leads to an orientation error relative to the face orientations needed to “close” the particle effective volume.

For the Hall problem, IG-SPH performs well (comparable to MFM). Standard SPH appears to capture the correct behavior but with surprisingly large noise in the diffusive case. This appears to be a direct consequence of the divergence-cleaning operators in SPH coupled to the inaccurate standard-SPH gradient estimator. Recall, we have not turned off “normal” MHD here, and divergence-cleaning is necessary for numerical stability but (as shown in Paper II) it introduces noise in the small-scale  $\mathbf{B}$ -field, which the standard SPH gradient estimator (given its low-order errors) is unable to correctly treat.

## 5.2 Diffusion Across a Moving, Rotated, Shearing Contact Discontinuity

We next consider a more challenging variation of the diffusion sheet, illustrated in Fig. 6. We (1) re-enable our normal MHD physics. (2) Insert a contact discontinuity at  $x = 0$  (the location of the jump in  $\mathbf{q}$ ) with a density jump of a factor of 2, so the diffusion (of some passive scalar) is across the discontinuity. This implies a different particle arrangement (since our particles are equal-mass) across  $x = 0$ . (3) Make the discontinuity shearing, with  $v_y = x/2$ . This means the particle geometry around the diffusing interface is constantly being re-arranged. (4) Uniformly boost the system by  $\mathbf{v}_{\text{boost}} = (10, 3, 2) c_s$ . (5) Rotate the entire system by  $+35^\circ$ .

None of these changes the physical solution for the diffusion. However they are all, in principle, numerically challenging. Because our methods are fully Lagrangian, our solutions are trivially invariant to the boost (4) and rotation (5) operations. This is not the case, however, for Eulerian methods. Our MFM method is also invariant to (1) and (2), i.e. the evolution of a stable contact discontinuity produces vanishing fluxes, and the gradient estimator is

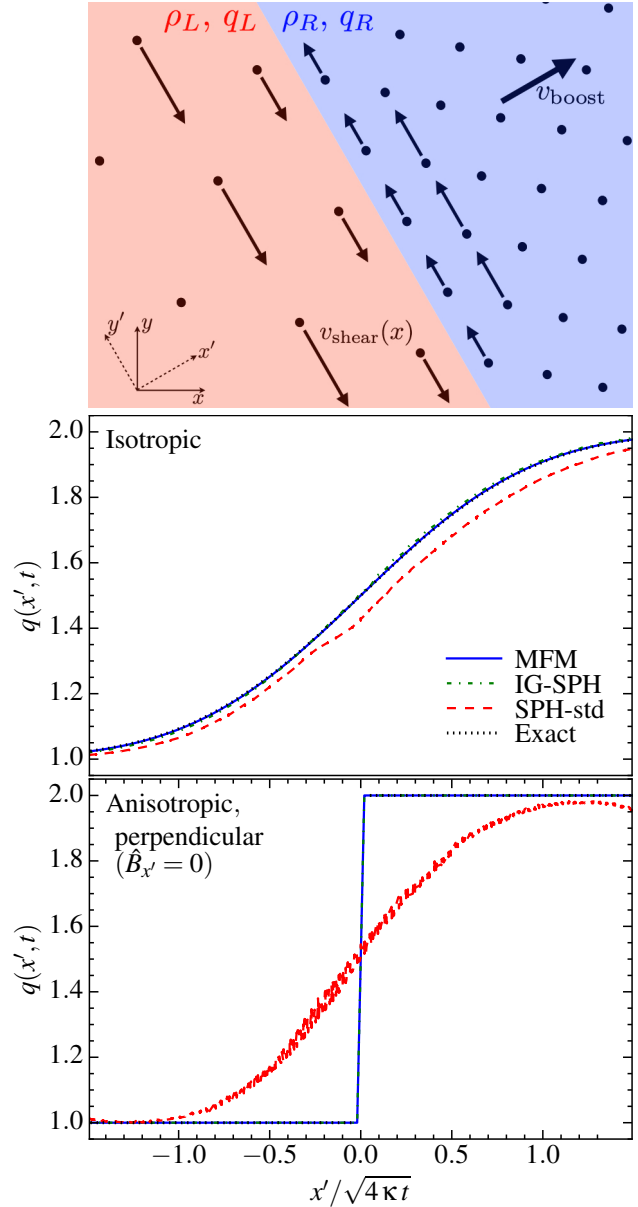


**Figure 6.** Diffusion across a super-sonically moving, rotated, shearing contact discontinuity (§ 5.2), as Fig. 1, with full MHD physics enabled. *Top:* Illustration of the initial problem setup. We measure properties along the  $x'$  axis, perpendicular to the initial discontinuity in density and  $\mathbf{q}$ . We consider an isotropic case (*middle*) and an anisotropic, perpendicular (fully-suppressed; *bottom*) case. The contact discontinuity means the particle arrangement is different on either side of  $x' = 0$ , and the shear field means that the arrangement of neighbor particles is constantly changing. MFM and IG-SPH agree well with the exact solution. In standard SPH, the particle-density gradient produces a systematic gradient error that leads to the  $+x'$  offset in the isotropic case; in the anisotropic case, we again see SPH over-diffuse (with some additional noise here).

explicitly insensitive to particle arrangement within the kernel for linear gradients. This is not the case, however, in SPH, where the solutions around contact discontinuities depend on the particle arrangement, and certain spurious forces can appear (see references in § 1).

Fig. 6 shows that, despite these complications, our MFM solution still agrees very well with the exact result. There is some noise around  $x = 0$ , introduced by the shear (3), particularly around the contact discontinuity, but it is not visible on the scale plotted.

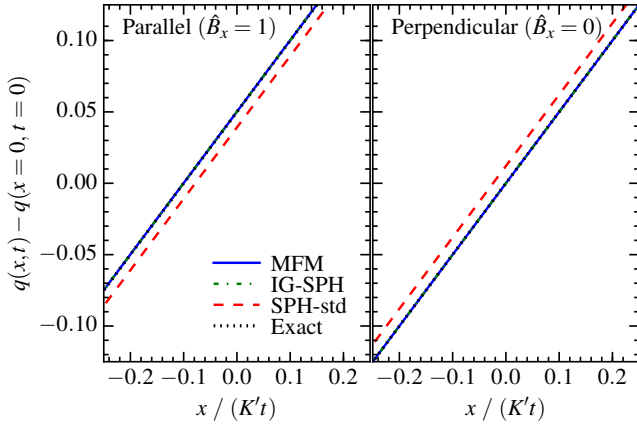


**Figure 7.** Diffusion with a variable diffusivity  $\mathbf{K}$  and diffused quantity  $q$  (§ 5.4). Both vary linearly in  $\hat{x}$ . The box is 3D with  $N = 64$  elements across the  $x$ -range, but the results are converged (up to tested  $N = 4096$ ). We consider anisotropic cases with parallel (*left*; no suppression) and perpendicular (*right*; full suppression) fields. MFM and IG-SPH agree well with the exact solutions; standard SPH shows the same systematic errors as before.

This constant re-arrangement of the particles (hence constant re-arrangement of the effective faces and implicit mesh) introduces “grid noise” (for detailed discussion of this noise term see Duffell & MacFadyen 2014; Hopkins 2015b; Mocz et al. 2015; Pakmor et al. 2016). In our standard SPH formulation, we see a different systematic offset – this owes to the gradient estimator being zeroth-order sensitive to the particle arrangement, so it returns a systematically incorrect value around the contact discontinuity. This leads to a net flux to the  $+x$  direction (the direction of increasing density across the contact discontinuity). The “wiggle” visible at  $x \sim 0$  owes to this error trying to resolve itself outside of the discontinuity. IG-SPH resolves this and produces good results, although a very small systematic offset from the exact solution appears in the isotropic case, owing to the assumption that faces vectors always lie along inter-particle separation vectors.

A detailed comparison with grid-based methods is outside the scope of this paper; however, this problem is very challenging for such codes. A moving contact discontinuity, especially one not aligned with the grid, produces large numerical diffusivity at low resolution (see Hopkins 2015b; Springel 2010). Using ATHENA to run a version of this problem with anisotropic conduction, we find the numerical diffusivity exceeds the physical diffusion even in the isotropic case unless we use more than  $\sim 512$  elements across the plotted range (compared to 64 here); even higher resolution is required for the anisotropic case.

### 5.3 Sinusoidal Temperature Distribution

We have also considered a one-dimensional test problem in which a scalar  $q$  follows a sinusoidal distribution from Arth et al. (2014). This tests the same physics as the later stages of the diffusing sheet, but is much “easier” (since it is 1D and there is never a steep gradient). No other MHD physics are active, and we take a periodic box of unit length  $L = 1$ , with unit density and sound speed and  $\gamma = 5/3$ , with the physical solution

$$q(t, x) = \frac{3}{2} + \sin(2\pi x) \exp\left(-4\pi^2 K \hat{B}_x^2 t\right) \quad (62)$$

initialized at  $t = 0$ . We have confirmed (as expected) that all the conclusions from our diffusing sheet tests apply in this test, and our results for both “standard” and “error-corrected” SPH are identical to those in Arth et al. (2014). Not surprisingly the offset from the correct solution in “standard” SPH is smaller here than in our dif-

fusing sheet, and even numerically unstable formulations are well-behaved because the flow is sufficiently smooth (this also applies to the wave tests using the gradients-of-gradients SPH method in Wurster et al. 2014).

### 5.4 Variable Diffusivity

We previously took  $\mathbf{K}$  to be constant. Here, consider the case  $q(x, t = 0) = q_0 + q'x$ ,  $K(x, t) = K_0 + K'x$ ; this produces the analytic solution  $q(x, t) = q(x, t = 0) + q'K't$ . In the simple anisotropic case with  $\mathbf{K} = K\hat{B} \otimes \hat{B}$  this becomes  $q(x, t) = q(x, t = 0) + |\hat{B}_x|^2 q'K't$ . We consider this in the same 3D box setup as before (here with large enough distance in the  $x$ -direction so that the boundary conditions do not enter the considered domain).

The results are shown in Fig. 7. All methods correctly treat the isotropic case (not shown). In the anisotropic case, MFM/MFV/IG-SPH perform well while standard SPH features similar systematic errors to the diffusing sheet.

### 5.5 Gaussian Pulse

We now consider a true multi-dimensional problem – the diffusion of a quantity injected as a  $\delta$ -function instantaneously into a homogenous background. In a periodic box of unit size, we initialize a 3D, spherically-symmetric Gaussian for  $q$  centered on the origin, where the diffused quantity is treated as a passive scalar with all other background properties constant (so no other MHD effects appear). In the isotropic case, this evolves as:

$$q(\mathbf{x}, t) = \frac{q_0 (2\pi)^{-3/2}}{(\epsilon^2 + 2\kappa t)^{3/2}} \exp\left[-\frac{1}{2} \left(\frac{x^2 + y^2 + z^2}{\epsilon^2 + 2\kappa t}\right)\right] \quad (63)$$

where  $q_0$  is an arbitrary normalization,  $\kappa$  is the diffusivity,  $t$  the time since the problem was initialized, and  $\epsilon$  defines the initial width of the distribution ( $\epsilon \rightarrow 0$  becomes a  $\delta$ -function; larger  $\epsilon$  correspond to starting from an already-evolved solution). We take  $\epsilon = 0.05$ , comparable to our inter-particle spacing, so that there is a well-defined gradient in our initial condition.

In the anisotropic case, if we assume  $\mathbf{K} = K\hat{B} \otimes \hat{B}$  with constant (in space and time)  $\hat{B}$ , we can always define our axes so that  $\hat{B} = \hat{x}$ ; then this evolves as:

$$q(\mathbf{x}, t) = \frac{q_0 (2\pi)^{-3/2}}{\epsilon^2 (\epsilon^2 + 2\kappa t)^{1/2}} \exp\left[-\frac{1}{2} \left(\frac{x^2}{\epsilon^2 + 2\kappa t} + \frac{y^2 + z^2}{\epsilon^2}\right)\right]$$

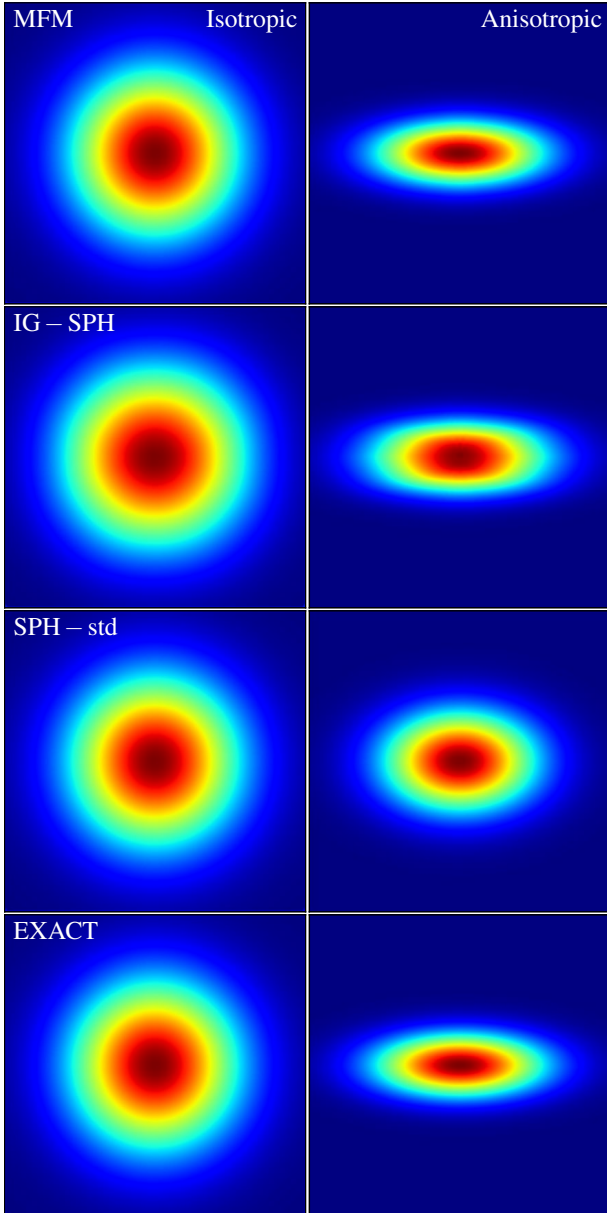
i.e.  $q$  diffuses normally along  $\hat{B}$ , and not perpendicular.

Fig. 8 shows the results for both MFM, IG-SPH and standard SPH in isotropic and anisotropic cases. In the isotropic case, all recover the solution accurately even at low resolution. In the anisotropic case, MFM and IG-SPH capture the anisotropy; standard SPH systematically (at all resolutions) only suppresses the perpendicular diffusion by a factor  $\sim 4 - 6$  (similar to the previous cases).

Note that in MFM and IG-SPH, the agreement here at low resolution (a  $64^3$  box) is not perfect, as some artifacts from the grid structure (here particles laid in a Cartesian grid) are visible in IG-SPH (they are much smaller, but still present, in MFM). These are invisible by-eye if we go to  $> 256^3$  resolution. We find that in truly multi-dimensional problems such as this, the perpendicular width of structures must be a few particles across before complete anisotropy can be fully captured. This is required so that a reliable gradient in the relevant direction can be determined (similar to the requirement in grid-based codes).

### 5.6 Diffusing Ring

A more challenging version of this problem is diffusion with azimuthal anisotropy, following Parrish & Stone (2005); Sharma &



**Figure 8.** Three-dimensional Gaussian pulse test (§ 5.5). A Gaussian distribution of the diffused quantity  $q$  is injected at the center with initial spherically symmetric width  $\epsilon = 0.05$ . We plot a slice through the  $x - y$  plane, at time  $t = 0.8$  for diffusivity  $K = 0.01$ , in a box of unit size with  $128^2$  elements. *Left:* Isotropic diffusion. The Gaussian simply expands; all methods accurately capture the exact solution (*bottom*). *Right:* Anisotropic diffusion with  $\mathbf{K} = K \hat{B} \otimes \hat{B}$  and  $\hat{B} = \hat{x}$ . The distribution should expand only in the  $x$ -direction. MFM and IG-SPH capture this, with minor artifacts from the initial particle arrangement which converge away at higher resolution. Standard SPH produces a perpendicular diffusion which is only a factor of  $\sim 4$  lower than the parallel diffusion; this error does not converge away.

Hammett (2007, 2011). In a periodic box of unit size centered on the origin and cylindrical  $(r, \phi, z)$  coordinates,  $\rho = u = 1$ ,  $\mathbf{v} = 0$ , and purely azimuthal magnetic fields  $\mathbf{B} = B_0 \hat{\phi}$ , we initialize  $q(t=0) = q_0 + q_1 (\exp[-(1/2)[(r-r_0)^2/\delta r_0^2 + \phi^2/\delta\phi_0^2])$ . Here  $q_0$  and  $q_1$  are an arbitrary background and normalization (we take  $q_0 = 10^{-10}$  and  $q_1 = 1$ ),  $\delta r_0 = 0.05$  and  $r_0 = 0.3$  define a Gaussian ring at radius  $r_0$  of width  $\delta r$ , and  $\delta\phi_0 = 0.5$  is an initial Gaussian spread about  $\phi = 0$  in the  $\hat{\phi}$  direction. We assume  $\mathbf{K} = K \hat{B} \otimes \hat{B}$ .

Because the fields are purely azimuthal, the quantity should diffuse in the purely azimuthal direction, “around the ring,”

rather than in the radial direction. At early times, this has an exact solution of the same functional form:  $q(t > 0) = q_0 + q_1(t) (\exp[-(1/2)[(r-r_0)^2/\delta r_0^2 + \phi^2/\delta\phi^2])$  where  $\delta\phi^2 = \delta\phi_0^2(r, t) = \delta\phi_0^2 + 2K r^{-2} t$  (with normalization  $q_1(r; t) = q_1(t=0) (\delta\phi_0/\delta\phi)$ ). This assumes we can neglect the periodic boundary conditions around the ring – i.e. is valid for  $\delta\phi \ll \pi$  (hence early times). At late times, the diffusion from both directions self-intersects on the opposite side of the ring, and there is no simple exact solution. Eventually, though, as  $t \rightarrow \infty$ , the system becomes isothermal within each azimuthal annulus. This is a challenging problem even in high-order grid codes (see Parrish & Stone 2005).

Fig. 9 compares the results at early and late times, at two different resolution levels. As before, MFM and IG-SPH are able to capture the azimuthal anisotropy. Even at low resolution ( $64^2$ ), there are only weak grid artifacts, but these and the amount of perpendicular diffusion improve at higher resolution. At late times, for comparison, in the fixed-grid code ATHENA on a Cartesian mesh (where the preferred direction of the grid is not the azimuthal direction), it requires going to  $\sim 256^2$  resolution before the diffusion properly “wraps” into a ring at all (see e.g. Sharma & Hammett 2011); our  $128^2$  case resembles a  $\sim 512^2$  case with ATHENA. And we note that we have not aligned the particles with the anisotropy (the particles are in a regular triangular lattice).

On the other hand, standard SPH (Fig. 10) clearly exhibits excessively isotropic diffusion, even at early times. At late times that error dominates the solution. We see no evidence that this error converges away at higher resolution.

Note that we have tested both the 2D ring version of this problem and the 3D version, where the ring becomes a cylinder elongated in the  $\hat{z}$  direction and the box is periodic in that direction. The results are very similar in both cases.

### 5.6.1 Alternative SPH Formulations

We have also tested the alternative standard SPH formulations from § 3.2 in the diffusing ring problem. Unless we use “perfect” initial conditions (a regular particle lattice and zero noise), all of the alternative formulations are numerically unstable and the errors (while smaller at  $t \lesssim 0.2$  grow and become catastrophic by  $t \sim 1$  (either crashing the code or giving un-physical solutions). With flux-limiters included to eliminate the instability, the results are qualitatively the same as the “standard SPH” example in Fig. 9.

Of all the “non-IG” SPH variants, we find the best behavior with the flux-limited “gradients of gradients” SPH method (much better than our default SPH-std). If we start from perfect ICs with a sufficiently smooth initial gradient, we can also use the un-limited gradients-of-gradients method. However, in both cases there are still errors which do not converge except with increasing neighbor number, and at all resolutions and neighbor numbers we explore this method is still less accurate than our IG-SPH method.

### 5.6.2 Convergence

Note that our diffusing ring setup is slightly different from that in Sharma & Hammett (2007, 2011); Kannan et al. (2015), who used this problem to measure the convergence properties of their method. We have therefore also compared initial conditions which match their choice: we initialize a step-function discontinuity with  $q = q_0$  and  $q = q_1$  inside or outside (respectively) of an annulus  $0.25 < r < 0.35$  and  $-\pi/6 < \phi < \pi/6$ . The qualitative results with all methods are identical to those shown in Figs. 9–10.

Fig. 11 quantifies the convergence (in 2D tests using this initial condition) by measuring the L1 norm of  $q$  at time  $t = 0.2$  relative

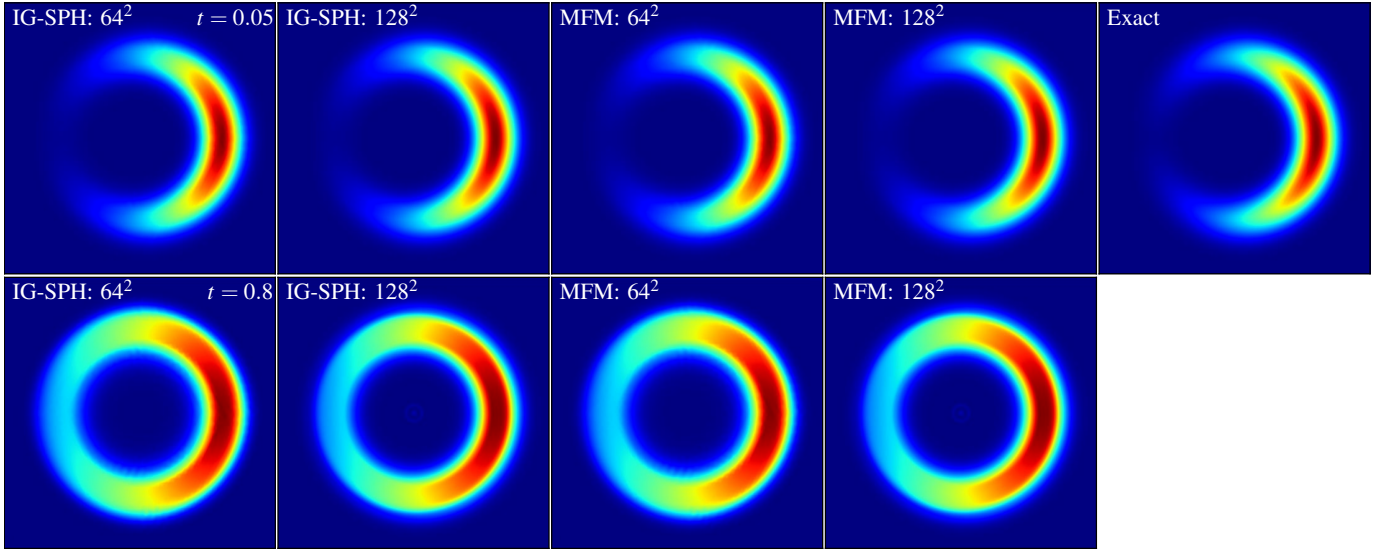


**Figure 9.** The diffusing ring test problem (§ 5.6). A “hot spot” (high- $|\mathbf{q}|$ ) within a small radial annulus is initialized with pure azimuthal fields; this should diffuse into a ring without additional radial diffusion. We compare IG-SPH and MFM at two different resolutions (labeled), and both early (*top*) and late (*bottom*) times. For early times there is an approximate analytic solution, shown; for late times there is no analytic solution, but the high- $|\mathbf{q}|$  material should remain confined to the same radial annulus as at early times, gradually diffusing around the ring until it is isothermal. In MFM/MFV/IG-SPH we see good agreement with the expected behaviors at both times, even at low resolution. There is some numerical radial diffusion, but this gradually converges away as we go towards higher resolution.

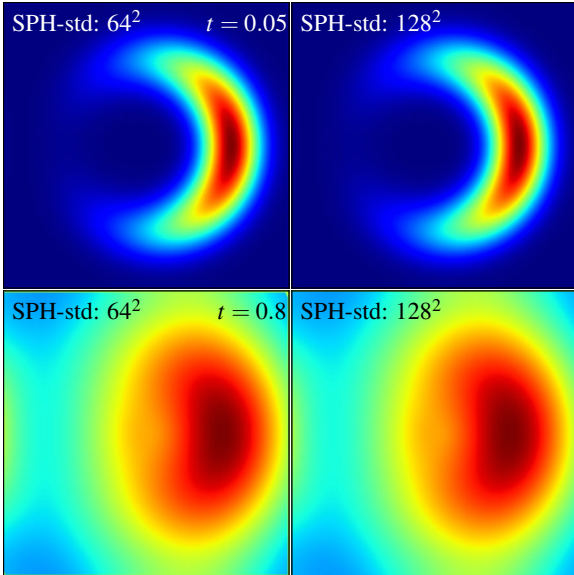


**Figure 10.** Diffusing ring test as Fig. 9, but for “standard” SPH. In all stable standard SPH variants considered in § 3.2, the perpendicular diffusion is only weakly suppressed and it dominates the solution at late times.

to a high-resolution solution ( $2048^2$ ) interpolated to the particle positions. We find a convergence rate  $L1 \propto N^{-0.9}$ , close to the ideal  $\propto N^{-1}$ . This is competitive with and in some cases superior to the implementations studied in fixed-grid and moving-mesh codes in Sharma & Hammett (2007, 2011); Kannan et al. (2015).

### 5.6.3 Tensor Diffusion: The Radiative Diffusion Case

Interestingly, if we consider the radiative diffusion version of this problem, the behavior is qualitative different. Take  $\mathbb{D}_\nu = \hat{n} \otimes \hat{n}$  and  $\hat{n} = \hat{\phi}$  (define  $K \equiv \lambda c / (\kappa_\nu \rho)$ ); because the anisotropy is *inside* the first gradient in the diffusion equation (i.e. we have  $\mathbf{F} = K \nabla \cdot [(\hat{\phi} \otimes \hat{\phi}) |\mathbf{q}|]$  as opposed to  $\mathbf{F} = K (\hat{\phi} \otimes \hat{\phi}) \cdot \nabla |\mathbf{q}|$ ), the solution is distinct. For an azimuthally symmetric  $\mathbf{U} = n_\nu = n_\nu(r)$  and  $\hat{n} = \hat{\phi}$ , the dif-

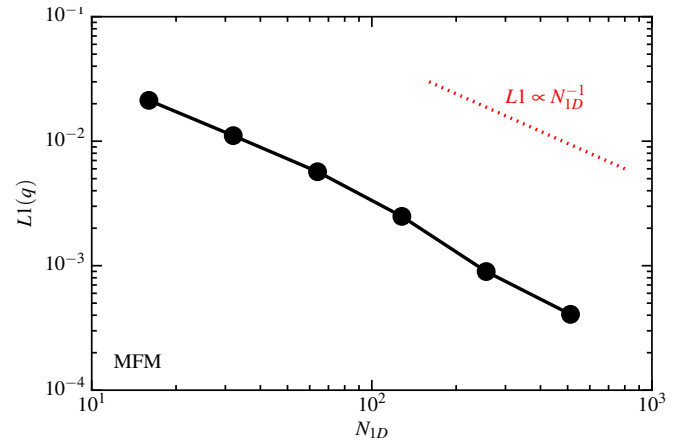


**Figure 11.** Convergence in the diffusing ring test (Fig. 9), with our MFM method (IG-SPH is similar). We plot the L1 error norm in  $q$  averaged over the domain as a function of the number of elements on a side  $N_{1D}$ , at a fixed time  $t = 0.2$ . Convergence is close to the ideal linear scaling (dotted red). Standard SPH exhibits a flat scaling (no convergence), with L1 errors larger than the maximum shown in this plot.

fusion equation for scalar  $q$  reduces to  $\partial q / \partial t = -(K/r) \partial q / \partial r$ , i.e. the ring expands radially with a speed  $= K/r$ .

Fig. 12 shows the results of this test. In our MFM/MFV/IG-SPH methods, the ring expands as expected. This behavior is captured qualitatively even at extremely low resolution ( $\sim 32^2$ ). There is slightly more perpendicular diffusion at fixed resolution in IG-SPH. As expected SPH-std fails to capture the correct behavior – the extra isotropic diffusion “fills in” the interior of the ring, and the dependence of the SPH gradient estimator on the particle arrangement breaks the circular symmetry of the ring.

## 5.7 Anisotropic Diffusion-Driven Instabilities: MTI & HBI

We now consider two instabilities specific to anisotropically conducting plasmas: the magneto-thermal instability (MTI) and heat-

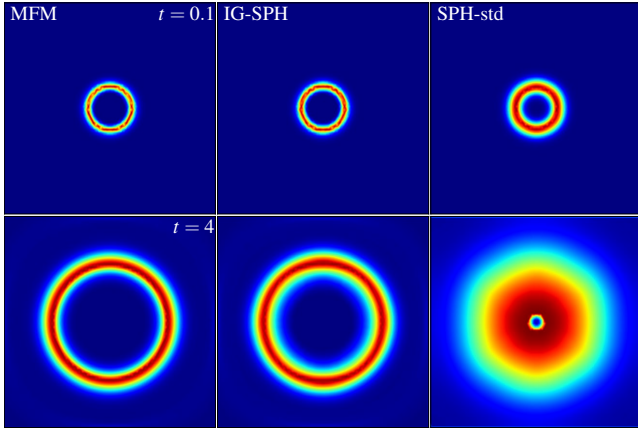


**Figure 12.** Diffusing ring test for radiative diffusion (§ 5.6.3), where the diffused quantity  $\mathbf{q} = q\mathbb{D}_\nu$  is an anisotropic tensor, with  $\mathbb{D}_\nu = \hat{\phi} \otimes \hat{\phi}$  (i.e. a purely azimuthal Eddington tensor). We initialize a small ( $r = 0.1$ ), thin ( $\delta r = 0.01$ ), azimuthally symmetric ring (in a box of unit length); the ring should expand with speed  $\approx K/r$  and remain thin. The resolution here is  $64^2$ , and we show the result at early ( $t = 0.1$ ; *top*) and late ( $t = 4$ ; *bottom*) times. MFM and IG-SPH capture the physically correct behavior, with slightly larger perpendicular diffusion in IG-SPH (reflected in the slightly more extended “tails” inside/outside the ring). Standard SPH produces an isotropic-like diffusion that (incorrectly) fills in the ring.

flux driven buoyancy instability (HBI) (Balbus 2000; Quataert 2008). These have been studied in various astrophysical contexts as drivers of turbulence, convection, and mechanisms to enhance or suppress conduction; our specific problem setup is motivated by the studies in Parrish & Stone (2005); Parrish et al. (2008); Parrish & Quataert (2008); McCourt et al. (2011); Kannan et al. (2015).

Here, we are not interested in the physics of the instabilities themselves, but they are useful numerical tests for several reasons. (1) They require accurate coupling of the anisotropic conduction to the magneto-hydrodynamics of the flow (not guaranteed in operator-split methods). (2) They are specific to anisotropic conduction and are suppressed with isotropic conduction, so directly test whether isotropic numerical diffusion can overwhelm physical diffusion. (3) They test the ability of the anisotropic conduction operator to recover small-amplitude seed perturbations. (4) They lead to non-linear, sub-sonic turbulence, which is particularly challenging for mesh-free methods and especially SPH to treat accurately (see e.g. Kitsionas et al. 2009; Price & Federrath 2010; Bauer & Springel 2012; Sijacki et al. 2012), and require that our operator preserves anisotropy even in a turbulent flow.

### 5.7.1 High-Resolution Tests

Following Parrish & Stone (2005); Parrish et al. (2008); Parrish & Quataert (2008); McCourt et al. (2011); Kannan et al. (2015), we initialize a 2D box in  $x-z$  coordinates with an analytic constant gravitational acceleration  $\mathbf{g} = -\hat{z}$ , size  $L = 1/10$ , resolution  $256^2$ , polytropic  $\gamma = 5/3$ , and conductivity  $K = 0.01$  ( $\mathbf{K} = K\mathbf{I}$  for the isotropic case,  $\mathbf{K} = K\hat{B} \otimes \hat{B}$  for the anisotropic case). For the MTI, we initialize  $u = (3/2)(1 - z/H)$  with  $H = 3$ , and  $\mathbf{B} = 10^{-11}\hat{x}$ , with a seed velocity perturbation<sup>11</sup>  $\mathbf{v} = \mathcal{M}_0 c_s \sin(4\pi x/L)\hat{z}$  with

<sup>11</sup> In our high-resolution tests, we use a seed velocity perturbation with magnitude  $\mathcal{M}_0 = 10^{-2}$  instead of  $\mathcal{M}_0 = 10^{-4}$  as in Parrish & Stone (2005); Parrish et al. (2008); Parrish & Quataert (2008). This was chosen for computational convenience. Because we use an explicit integration method, the timestep for high resolution in a small spatial domain becomes very

$\mathcal{M}_0 = 10^{-2}$ . For the HBI,  $u = (3/2)(1 + z/H)$  with  $H = 2$ , and  $\mathbf{B} = 10^{-11}\hat{z}$  and  $\mathbf{v} = \mathcal{M}_0 c_s [\sin(3\pi z/L)\hat{x} + \sin(4\pi x/L)\hat{z}]$ . The density  $\rho(z)$  is initialized so that the initial pressure gradient balances gravity with  $\langle \rho \rangle = 1$  in the box. The domain is divided vertically into three equal sub-domains of length  $L/3$ ; the top and bottom layers have isotropic conduction (i.e. are buoyantly neutral) while the central layer has anisotropic conduction (this follows the previous studies and reduces the sensitivity to boundary conditions). The boundaries are periodic in  $\hat{x}$ ; and constant-temperature reflecting boundaries in  $\hat{z}$ .<sup>12</sup>

Both of these represent a stably stratified atmosphere. With no conduction, or isotropic conduction, the system should remain in equilibrium and the seed perturbations should damp. With anisotropic conduction, provided a large enough diffusivity (as chosen here) such that the system is approximately isothermal along field lines, the instabilities should grow and eventually re-orient the field lines. In the MTI (vertical temperature profile  $dT/dz < 0$ ), the small vertical velocity grows into large, non-linear convective cells which carry the field lines and re-orient the field in the vertical direction, until the cells cross the domain and the fixed-temperature boundary conditions produce sustained turbulence. In the HBI ( $dT/dz > 0$ ), the initial mixed perturbation generates growing separation/compression of field lines, which leads to horizontal motions that try to stretch the field lines horizontally, until the instability saturates when the field lines are horizontal and suppress further convection. In both the HBI and MTI, the characteristic timescale is the buoyancy time  $|g \partial \ln T / \partial z|^{-1/2} (\sim 1.7, 1.4)$  for MTI, HBI, respectively).

Fig. 13 shows the results of these tests at a few buoyancy times, using our MFM method. Recall the relatively large initial perturbation here means non-linear behavior can develop in just a couple buoyancy times, and we see that occur in the anisotropic case. The qualitative behavior of the non-linear HBI and MTI compares well to that seen in Parrish & Stone (2005); Parrish & Quataert (2008); McCourt et al. (2011). In both MTI and HBI, the cases with isotropic diffusion show (correctly) no evidence of instability, and the initial perturbations are eventually fully damped.

However, we do not see good behavior with SPH. We use a lower-resolution suite of tests to explore this more rigorously below.

### 5.7.2 Low-Resolution Tests

To quickly explore different numerical methods and the late-time evolution of the MTI and HBI, we also consider a low-resolution initial condition which is identical to our high-resolution tests, but with lower resolution  $32^2$  and larger box size  $L = 1$  (these both allow larger timesteps), smaller seed velocity  $\mathcal{M}_0 = 10^{-4}$ , and larger

short ( $\sim 10^{-5}$ ). Using the smaller seed velocity requires approximately an order-of-magnitude longer runtimes to develop non-linear behavior, so we adopt the larger seed for high-resolution tests. However we explicitly show in § 5.7.2 below that our MFM method can accurately capture very small seed velocities even at much lower resolution  $\sim 32^2$ .

<sup>12</sup> A sharp, reflecting and conducting “wall” is particularly challenging to implement in mesh-free methods. We treat the reflecting boundaries as follows: a layer (3 particles deep) of boundary particles with fixed positions and temperatures is placed at  $z < 0$  and  $z > L$ . For every interaction between a boundary particles and normal particle (gradient calculation, the hydrodynamic operations, etc), the boundary particle is assumed to have all specific properties matched to the normal particle, except the temperature (fixed to the IC value), velocity and magnetic field (which follow the usual reflection rules) and density (adapted to give equal pressure, given the different temperatures).

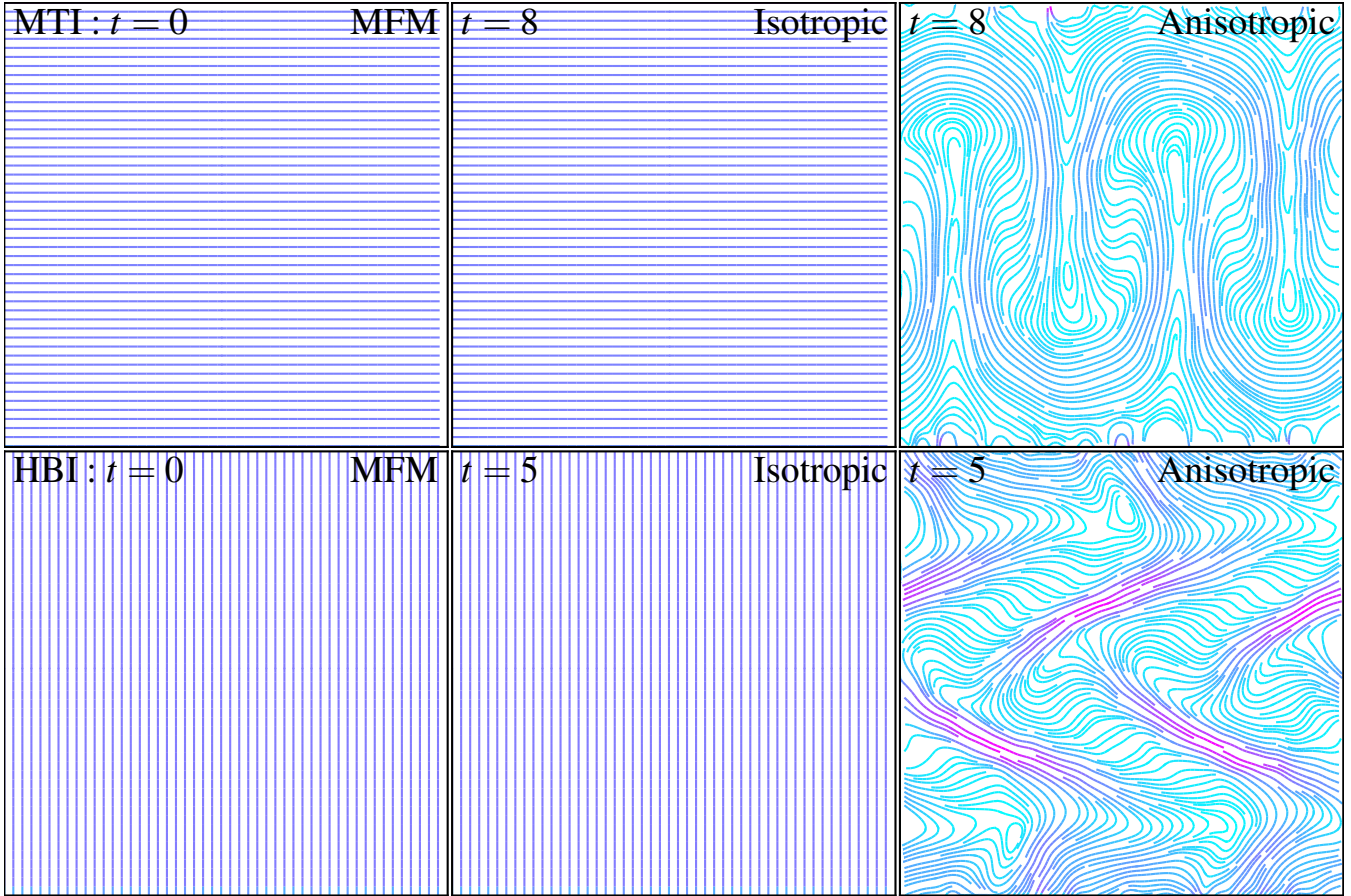


**Figure 13.** Magneto-thermal instability (MTI) and heat-flux driven buoyancy instability (HBI) tests (§ 5.7), with our MFM method. *Top:* MTI: The initial condition (*left*) is a 2D box of length  $L = 0.1$ , with  $256^2$  resolution elements, with a vertically stratified atmosphere with  $dT/dz < 0$  (temperature decreases upwards), in equilibrium with a constant vertical gravitational field  $\mathbf{g} = -\hat{z}$  and conductivity  $\kappa = 0.01$ . Magnetic field lines are shown at different times  $t$ ; these are initialized with trace values aligned along  $\hat{x}$ . With no diffusion, or isotropic diffusion ( $\mathbf{K} = \kappa \mathbf{I}$ ; *center*), the system is stable and the field configuration should be preserved. With anisotropic diffusion ( $\mathbf{K} = \kappa \hat{B} \otimes \hat{B}$ ; *right*), the system is unstable and develops convection. This re-orientates the field to be initially near vertical (at e.g. the time shown), then breaks up into turbulence and the field becomes isotropic. The characteristic timescale is the buoyancy time  $\sim 1.7$  in these units. *Bottom:* HBI. The resolution and conductivity are the same but the initial atmosphere now has  $dT/dz > 0$ , and initial  $\hat{B} = \hat{z}$ . Again with no diffusion or isotropic diffusion, the system is stable. With anisotropic diffusion, the HBI amplifies transverse motions that re-orient the field to be perpendicular ( $\hat{B} \rightarrow \hat{x}$ ). MFM recovers all of the expected behaviors for both instabilities with anisotropic diffusion, and correctly suppresses them with isotropic diffusion.

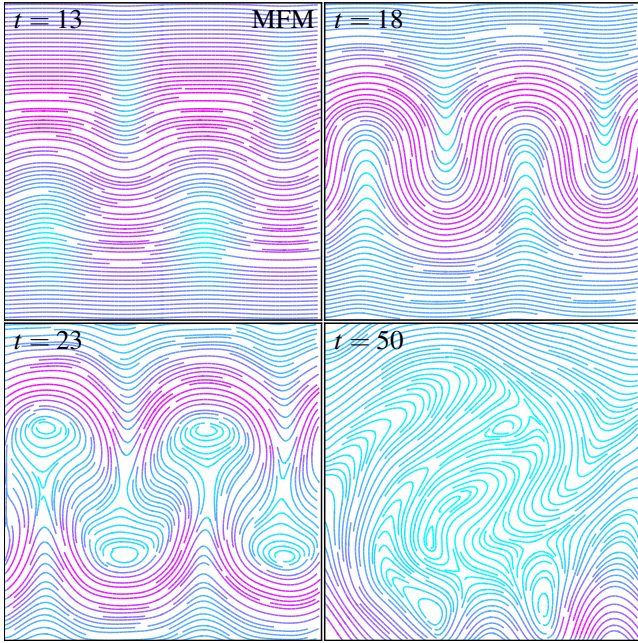
conductivity  $K = 0.1$  (to preserve the desired limit where the conduction is sufficiently fast).

Fig. 14 shows the time evolution of the MTI in one of these runs, with MFM. Fig. 15 compares different methods at fixed time. Quantitatively, Fig. 17 shows the volume-averaged Mach number and rms  $\hat{z}$  component of the magnetic field as a function of time.

In MFM, we see the instability grow (despite the very low resolution), going non-linear after  $\sim 10 - 20$  buoyancy times (similar to high-resolution cases with the same seed perturbation amplitude; Parrish & Stone 2005; McCourt et al. 2011; Kannan et al. 2015), at which point the convective plumes re-order the magnetic field from horizontal to vertical. At late times, the plumes break up into sustained, non-linear convection, which isotropizes the field (although this is known to be sensitive to the boundary conditions). The fluctuations around isotropy owe to the ongoing turbulence (and are smaller at higher resolution). The saturated Mach numbers  $\sim 0.01 - 1$  are larger than those in the smaller  $L = 0.1$  box, as expected based on the scaling seen in McCourt et al. 2011. Both qualitative and quantitative evolution compare favorably to higher-resolution studies in fixed-grid and moving-mesh schemes (McCourt et al. 2011; Kannan et al. 2015).

With “standard” SPH, the instabilities never develop. This is true even at higher resolution and SPH neighbor number (we tested  $512^2$  with 3D-equivalent of 400 neighbors and a Wendland C6 spline). The isotropic component of the diffusivity is simply too large, so prevents the instabilities. This is true of all the stabilized “standard SPH” implementations in § 3.2. The numerically unstable formulations of SPH all either exhibit catastrophic, runaway errors (when noise and turbulence seed numerically unstable terms), or systematically produce negative conductivity (essentially “time-reversing” the instabilities).

IG-SPH is able to capture some characteristics of the MTI, but is plainly corrupted by noise – this erroneously “jumps” the Mach number to  $\sim 0.01$  very quickly. The noise relates to a combination of the known zeroth-order SPH errors (in the MHD equations) and the SPH divergence-cleaning operator (which also, in concert with the boundary conditions, drives the deviation from isotropic fields); these same errors seed similar noise in other test problems including Kelvin-Helmholtz and the magneto-rotational instabilities (see Paper II). If we replace the MHD solver with MFM and use only the IG-SPH conduction operator, the noise is greatly dimin-



**Figure 14.** Development of the MTI in an MFM simulation at low ( $32^2$ ) resolution, now with a box of side-length  $L = 1$ . Field lines are shown as Fig. 13. Initially small seed velocity perturbations grow in the vertical direction and become the convective cells. Once the cells reach the box boundaries ( $t \gtrsim 25$ , the convection is sustained by the constant-temperature, reflecting boundary conditions and produces sustained turbulence that isotropizes the magnetic field. Again, MFM can capture all the important behaviors even at very low resolution, especially for the larger box studied here which produces larger Mach numbers (here  $\sim 0.03$ ) compared to Fig. 13. The buoyancy time for this setup is  $\sim 1.7$ .

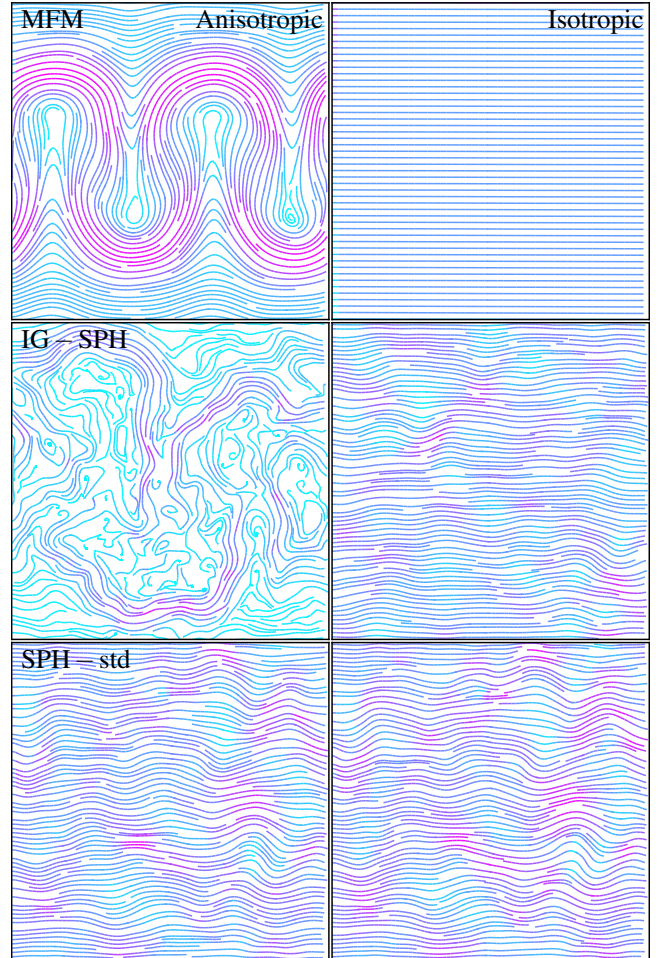
ished. Within SPH, we must go to higher resolution and increase the neighbor number, to slowly converge away the noise.

Fig. 16 shows the HBI with different methods, as Fig. 15; the quantitative results are again shown in Fig. 17. Even at low resolution MFM captures the instability (and suppresses it in the isotropic case). The instability goes non-linear on a similar timescale to the MTI, but the Mach numbers slowly decay as the field re-aligns. Interestingly, for the  $L = 1$  box, there is an intermediate period of isotropic fields, before the instability completes their horizontal re-alignment; this does not appear in the  $L = 0.1$  box, so we suspect it owes to the larger turbulent “overshoot” through the unstable zone induced by the first phase of the instability, which must be damped before the re-alignment can complete.

Neither IG-SPH nor standard SPH captures the HBI at this resolution. The HBI is more difficult in SPH because even in the larger box here, it is a highly sub-sonic instability; at any resolution, the artificial viscosity and conductivity “switches” in SPH, coupled to the kernel noise, can produce excessive isotropic diffusivity that suppresses the instability (see Paper 1).

## 5.8 Hall MRI

As discussed in § 5.1.5, the Hall effect presents unique numerical challenges; therefore, we now consider the magneto-rotational instability (MRI) with a Hall term and Ohmic resistivity (“Hall MRI”). This again involves the effects of anisotropic diffusion on plasma instabilities and turbulence. The effects of the Hall term is especially important in the context of proto-stellar and proto-planetary disks (for reviews, see Balbus 2003; Wardle 2007), and



**Figure 15.** Low-resolution MTI simulations with  $L = 1$  (as Fig. 14), with different methods using both anisotropic (*left*) and isotropic (*right*) diffusion. *Top:* MFM. The instability develops with anisotropic diffusion and is correctly suppressed with anisotropic diffusion. *Middle:* IG-SPH. The instability develops, but is corrupted almost immediately with large-amplitude noise (equivalent to few-percent Mach numbers). The noise owes primarily to the SPH MHD solver, not to the IG-SPH conduction solution; as such it converges only with increasing resolution and SPH neighbor number and does so slowly. The noise is also visible in the isotropic case: although the instability is suppressed, large fluctuations appear owing to numerical errors seeded by the initial modes. *Bottom:* Standard SPH. Noise is again present, but the instability never develops. The isotropic (perpendicular) diffusion is too large, and completely suppresses the instability. This is independent of resolution.

has been studied in detail using Eulerian methods (Flock et al. 2011; Simon et al. 2011; Bai 2011; Simon et al. 2015).

The MRI itself is astrophysically interesting in a wide range of contexts involving magnetized disks, and is numerically particularly interesting because it has historically proven challenging for SPH methods to correctly capture its growth (see e.g. Rosswog & Price 2007; Price & Bate 2008; Dolag & Stasyszyn 2009). In Paper II and Hopkins (2015a), we consider extensive studies of the MRI in ideal MHD ( $X_0 = 0$ ,  $\text{Re}_{M,0} \rightarrow \infty$ ) in GIZMO. We showed that our MFM and MFV methods recover the correct linear growth rates and non-linear properties in good agreement with well-tested higher-order Eulerian codes such as ATHENA. We also showed that improved SPH schemes were capable of doing the same (albeit with greater noise), but only if a large neighbor number ( $\gtrsim 128$  in 3D) is used to suppress the usual zeroth-order SPH errors.

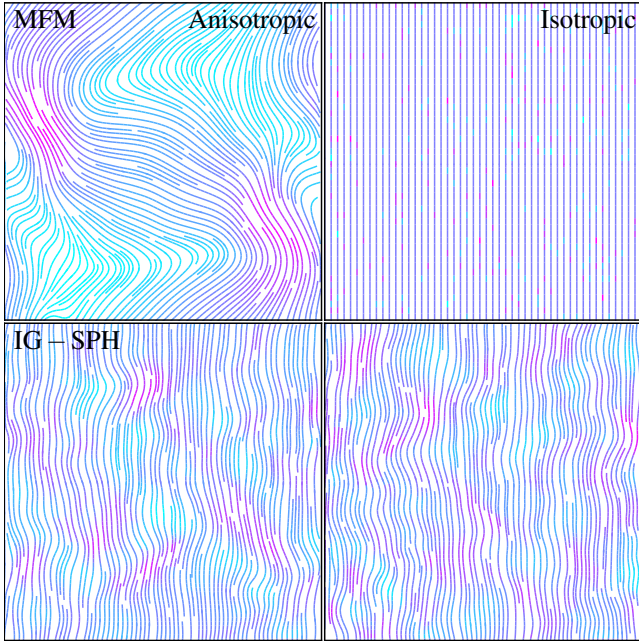


**Figure 16.** Low-resolution HBI simulations with  $L = 1$  (as Fig. 15), with different methods using both anisotropic (left) and isotropic (right) diffusion. *Top:* MFM. The instability develops with anisotropic diffusion and is correctly suppressed with anisotropic diffusion. *Bottom:* IG-SPH. Noise is present in both cases as with the MTI, but the instability never develops in the anisotropic case. The buoyancy time for this setup is  $\sim 1.7$ .

Here, we follow Sano & Stone (2002) and consider a simplified test problem. We adopt a 2D axisymmetric shearing box from Guan & Gammie (2008); this is locally Cartesian with one coordinate ( $x$ ) representing the radial direction and the other coordinate ( $z$ ) the vertical direction, representing a small, azimuthally symmetric “ring” about the midplane of a disk in a Keplerian potential. Details of the boundary conditions and gravitational terms, as implemented in GIZMO are in Paper II (this is the same box used for the MRI simulations therein). The box has initially constant density  $\rho_0 = 1$ , side-length  $L = 1 = H$  (where  $H \equiv (2/\gamma)^{1/2} c_{s,0}/\Omega$  is the scale-height), orbital frequency  $\Omega = 1$ , mean pressure  $P_0 = c_{s,0}^2/\gamma = \Omega^2/2$  ( $\gamma = 5/3$ ), spatially uncorrelated random pressure and velocity fluctuations with uniform distribution and  $|\delta P|/P_0 = |\delta \mathbf{v}|/c_{s,0} \leq 0.5 \times 10^{-2}$ , and uniform vertical field  $\mathbf{B} = B_0 \hat{z}$ . The MRI is then characterized by three numbers, the plasma beta  $\beta_0 \equiv P_0/(v_{A,0}^2 \rho_0) = 3200$  ( $v_{A,0} \equiv |B_0|/(4\pi \rho_0)^{1/2}$ ); the magnetic Reynolds number  $\text{Re}_{M,0} \equiv v_{A,0}^2/(\eta_0 \Omega) = 10$ , which determines the Ohmic resistivity  $\eta_0$ ; and the Hall parameter  $X_0 \equiv c B_0 \Omega / (2\pi e n_{e,0} v_{A,0}^2)$ , which determines  $\eta_H = |X_0| v_{A,0}^2 (2\Omega)^{-1} (|\mathbf{B}|/|B_0|) (\rho_0/\rho)$  (we assume the free electron fraction is constant).

Figs. 18-19 show the resulting evolution of the magnetic fields, for  $X_0 = +2, 0, -2, -5$ . For  $X_0 = 0$  (no Hall term), we simply have the MRI with explicit resistivity. In 2D shearing boxes, the fastest-growing modes for  $\text{Re}_{M,0} = 10 \gg 1$  should have growth rates only slightly smaller than the  $0.75\Omega$  expected in the ideal limit; once non-linear, they should form an inverse cascade until horizontal channel modes appear which grow without limit. For  $X_0 > 0$ , the behavior should be essentially identical, with slightly faster mode growth at higher  $X_0$ . When  $X_0 < -4$ , the system is fully stable against the MRI, and the initial perturbations should decay. At intermediate  $-4 < X_0 < 0$ , the MRI should grow but with a suppressed maximum growth rate (for finite  $\text{Re}_M$ ). Within this range, as

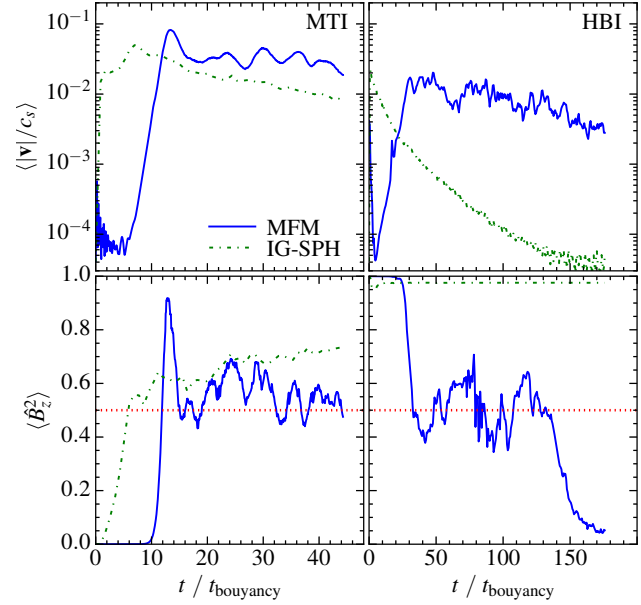


**Figure 17.** Time evolution of our low-resolution MTI (left) and HBI (right) simulations from Figs. 14-16. *Top:* rms Mach number (volume-averaged) in the center of the computational domain, as a function of time. *Bottom:* Mean squared  $z$ -component of the magnetic field orientation,  $\hat{B}_z^2 = (\hat{\mathbf{B}} \cdot \hat{z})^2$ . In MFM, the instabilities develop and velocities increase from their seed values rapidly around  $t \sim 10 - 20 t_{\text{buoyancy}}$ . The magnetic fields are rapidly re-oriented at the same time. In the MTI, fields go from horizontal to vertical, then the sustained convection with steady-state Mach numbers  $\sim 0.03 - 0.1$  (given the large box-size  $L = 1$ ) isotropizes the fields (red dotted line represents isotropic fields). The fluctuations about isotropy owe to the low resolution. In the HBI, fields go from vertical to isotropic, but the large Mach numbers ( $\sim 0.02$ ), low resolution, and boundary conditions here cause an overshoot that sustains fluctuations around isotropy until the velocities decay to  $\lesssim 0.01 c_s$ , at which point the instability rapidly completes the horizontal re-orientation of the field. In SPH, low-order MHD errors source large-amplitude velocity noise immediately, which corrupt the MTI. The seed velocities and noise are damped in the SPH-HBI case, and never drive the instability.

$X_0$  becomes more negative (larger  $|X_0|$ ), smaller-scale modes grow faster, until for  $X_0 \lesssim -2$  there is no critical scale at all; because of this, the system can saturate for many orbital periods with steady-state MRI turbulence (as the growing small-scale, high- $k$  modes prevent the formation of low- $k$  channel modes).<sup>13</sup>

In MFM, all of these behaviors are confirmed (compare Fig. 5 in Sano & Stone 2002). As expected and shown in detail in Paper II, the linear growth rates are suppressed at very low resolution ( $\sim 32^2$ ), but rapidly approach the analytic solution at higher resolution.

In IG-SPH, with neighbor number set to the same as our

<sup>13</sup> Note that, for  $-4 < X_0 < 0$ , given our setup, the instantaneous Hall parameter  $X \propto |\mathbf{B}|^{-1}$  and magnetic Reynolds number  $\text{Re}_M \propto |\mathbf{B}|^2$ , so as modes grow non-linear ( $|\mathbf{B}|$  increases), the system moves closer to the ideal MHD limit. Because our problem has finite  $\text{Re}_{M,0} = 10$ , if we begin with  $-2.1 < X_0 < 0$ , there is a fastest-growing mode, with relatively large wavelengths ( $\lambda_{\text{max}} \approx 0.03H, 0.09H$  for  $X_0 = -2, -1$ ). During the turbulent phase, these modes can increase  $|\mathbf{B}|$  non-linearly, which in turn increase the fastest-growing mode growth rate and wavelength, and suppress the growth of the smaller-scale modes. This can eventually trigger a runaway inverse cascade that produces the channel modes seen for  $X_0 \geq 0$ . We find that, if  $\lambda_{\text{max}}$  is well-resolved, this occurs eventually if  $X_0 \geq -2$  (for  $\text{Re}_{M,0} = 10$ ), although it in some cases requires  $\sim 100$  orbital times. For  $X_0 < -2.1$ , we confirm the turbulence remains essentially indefinitely.

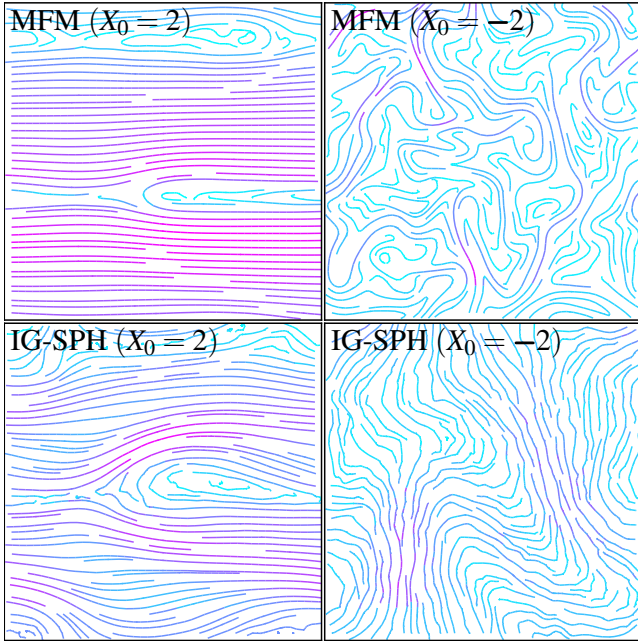


**Figure 18.** Hall MRI tests (§ 5.8). We compare the field lines (as Fig. 13) well into non-linear evolution for both MFM (*top*) and IG-SPH (*bottom*). The initial condition is a 2D  $R-z$  shearing box of length  $L = H$  (the pressure scale length) with  $128^2$  resolution, a constant field  $B_0 \hat{z}$ , trace pressure/velocity perturbations, and explicit Ohmic resistivity (with magnetic Reynolds number  $\text{Re}_{M,0} = 10 \times 1/\eta_0$ ) and Hall effects (with Hall parameter  $X_0 \propto 1/\eta_H$ ). Opposite signs of  $X_0$  correspond to the identical set-ups with opposite signs of  $\mathbf{B}$ ; this has no effects unless the Hall term is present. Results are shown at  $t \approx 6t_{\text{orbital}}$  ( $t_{\text{orbital}} = 2\pi/\Omega$ ), except for IG-SPH with  $X_0 = -2$ , where the mode growth is slow so results are shown at  $t \approx 12t_{\text{orbital}}$ . *Left:* For  $X_0 \geq 0$ , modes should grow quickly. In the non-linear state, the fastest-growing modes become bigger than the box, leading to the horizontal channel modes seen; these increase  $|\mathbf{B}|$  without limit. Qualitatively, both MFM and IG-SPH recover this. *Right:* For  $-4 \lesssim X_0 \lesssim -2$ , growth is slower and smaller modes grow fastest, leading to near-isotropic MRI turbulence in the saturated state as opposed to channel modes. MFM captures this. In IG-SPH, the small-scale modes are suppressed by low-order SPH errors and noise, so the correct small-scale vorticity fails to develop.

MFM/MFV runs (equivalent to 32 in 3D), we do not see growth of the MRI for any  $X_0$  (consistent with our results in Paper II and other studies, e.g. Tricco & Price 2012), unless we make the seed fluctuations significantly larger ( $\sim 10\%$ ). We therefore do not show these results. If we increase the neighbor number to a 3D-equivalent 128 (using a higher-order quintic spline for the kernel function), then we do recover MRI growth for small seed amplitudes. However, the behavior is problematic. For  $X_0 \geq 0$ , the correct (channel-mode) non-linear solution is eventually found, but the growth goes through multiple “plateau” phases where it is trapped in MRI turbulence before growing again. For  $X_0 < -4$ , the system does not exhibit runaway growth, but there is a much slower, steady monotonic growth of the azimuthal field amplitude (with  $e$ -folding time  $\sim 10t_{\text{orbital}}$ ; visible as the very slow rise in  $|\mathbf{B}|^2$  in Fig. 19), when there should be decay instead. These effects appear to owe to the much larger small-scale noise in  $\mathbf{B}$  present in SPH, which creates artificially-growing resolution-scale modes that can corrupt the longer-wavelength modes. For  $X_0 \approx -2$ , we do see saturation of the MRI; however, it is clear from the field lines in Fig. 18 that this is not a true turbulent flow (just a couple of large eddies). The small-scale noise is also evident in Fig. 18. The failure to capture small-

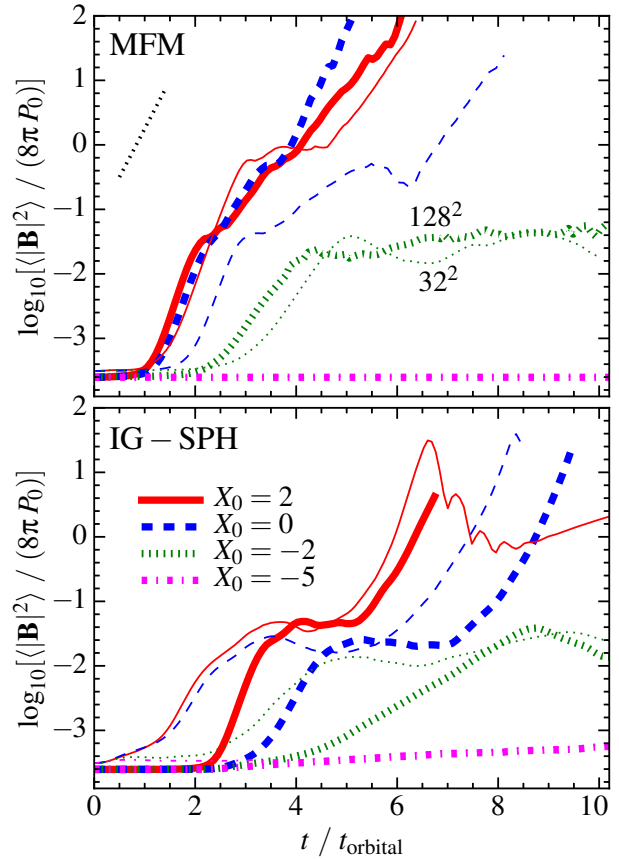


**Figure 19.** Growth of the volume-averaged magnetic pressure (relative to the initial thermal pressure  $P_0$ ) in the mean-field Hall MRI tests. We compare MFM (*top*) and IG-SPH (*bottom*). We show results for different initial Hall parameters  $X_0 = +2, 0, -2, -5$  (as labeled), at low resolution ( $32^2$ ; thin lines) and intermediate resolution ( $128^2$ ; thick lines). We also show the expected analytic maximum linear growth rate ( $|\mathbf{B}|^2 \propto \exp(1.5t)$ ; dotted black line), which should be close to the simulated growth rate for  $X_0 \geq 0$ . *Top:* In MFM, the growth for  $X_0 \geq 0$  is similar to the ideal MHD case (as expected), with growth rates in good agreement with the analytic expectation for  $128^2$  resolution, and late-time formation of channel modes (Fig. 18). Growth rates are suppressed at very low resolution, as expected from the MRI studies in Paper II. For  $X_0 = -2$ , linear growth is suppressed and the magnetic field strength saturates when the system saturates in MHD turbulence (also as expected). For  $X_0 = -5$ , the system should be stable against MRI growth; we confirm this and that the initial seed noise damps at the expected rate (decay rate  $\sim \Omega$ ). All the results here are in good agreement with well-tested Eulerian codes (see e.g. Sano & Stone 2002, Fig. 5). *Bottom:* In IG-SPH, some results are recovered but others are not. The initial growth is dominated by SPH grid-scale noise; this is why the modes grow immediately non-linear at low resolution, and more slowly at higher resolution. For  $X_0 \geq 0$  the channel modes develop, but growth is delayed by “plateau” phases of turbulence sourced by grid noise (this can even cause decay of the channel modes, seen for  $X_0 = 2$ ). For  $X_0 = -2$  the total magnetic pressure saturates but the small-scale turbulent structure is suppressed (Fig. 18). For  $X_0 = -5$  the modes do not grow rapidly, but they do grow slowly (growth rate  $\sim 50\Omega$ ), instead of decaying as they should.

scale turbulent structure in sub-sonic turbulence (the case here) is a well-known problem in SPH (see Paper I and Kitsionas et al. 2009; Price & Federrath 2010; Bauer & Springel 2012). In all cases, we see much faster initial growth for  $32^2$  resolution compared to  $128^2$ ; this is because the initial growth is entirely dominated by the large resolution-scale SPH noise (hence larger at low resolution), as we saw with the MRI and HBI in Fig. 17.

Finally, we note that we have re-run every problem in Sano &

Stone (2002) with our MFM method (varying  $\beta_0$ ,  $\text{Re}_{M,0}$ ,  $X_0$ , and the box size; considering zero net-field cases; and their whistler wave test problem) and confirm identical qualitative behavior.

### 5.9 Other Multi-Physics Problems

We have also vetted our algorithms in other non-linear problems where diffusion is not necessarily the primary physics. For example, we have considered a Sedov-Taylor blastwave with thermal conduction, and a shocktube with physical viscosity following (Sijacki & Springel 2006). We find good agreement between our MFM method and ATHENA, and the same systematic errors in standard SPH. The small differences between MFM and ATHENA at low resolution are dominated by the known numerical differences in their solution of the normal MHD equations (see Paper I-Paper II), not the sub-dominant diffusion terms. Therefore we do not consider these problems good tests of the diffusion treatment in itself (and do not study them further here). But they do serve as a validation that the diffusion operators here behave properly when coupled to additional dynamics.

A methods paper specifically devoted to the implementation of radiation transport is in preparation, where we compare the flux-limited diffusion, optically-thin variable Eddington tensor (OTVET; Gnedin & Abel 2001), and M1 moment closure approximations and consider several dynamical test problems designed to study the radiation-hydrodynamics of ionizing photons (Khatami et al., in prep). A similar detailed study of the cosmic ray implementation, including cosmic ray pressure effects and the role of cosmic ray streaming (as well as diffusion) is also in preparation (Chan et al., in prep).

As a “stress test” of our implementations, we have also run full cosmological simulations of galaxy formation using the Feedback in Realistic Environments (FIRE) models (Hopkins et al. 2014; Faucher-Giguere et al. 2015; Ma et al. 2015, 2016; Chan et al. 2015; Muratov et al. 2015; Oñorbe et al. 2015), with GIZMO in its MFM mode. These simulations include gas, stars, super-massive black holes, and dark matter, self-gravity, cosmological integrations, cooling physics and gas chemistry, star formation, and feedback from stars in the forms of photo-heating, radiation pressure, stellar winds, and supernovae. We have considered cases both with and without non-ideal MHD and with and without cosmic rays, using the Spitzer-Braginskii coefficients for anisotropic conduction and viscosity and Smagorinski eddy diffusion for metals. The results will also be the subject of future work (Su et al., in prep); for our purposes here, since there is no known “right” answer for such simulations, we consider these only to be useful tests of numerical stability under extreme conditions. Critically, we see no evidence for numerical instability or unphysical features owing to the addition of anisotropic diffusion operators in these simulations.

## 6 DISCUSSION

We present numerical discretizations of general anisotropic tensor diffusion operators for Lagrangian hydrodynamics methods, specifically for both recently-developed meshless finite-mass or finite-volume (MFM/MFV) Godunov schemes, as well as smoothed-particle hydrodynamics (SPH). We implement these in the multi-method code GIZMO, with the specific implementations relevant for passive scalar diffusion, non-ideal MHD (Ohmic resistivity, the Hall effect, and ambipolar diffusion), sub-grid “turbulent eddy diffusion” models, anisotropic conduction and viscosity (shear/bulk or Braginskii), cosmic ray diffusion and streaming, and anisotropic radiation diffusion (with a variable Eddington tensor).

We consider a variety of test problems. In all cases, our finite-element MFM/MFV schemes can produce accurate solutions, even at low resolution, and are numerically stable. The schemes are also manifestly conservative. They are able to recover correctly the anisotropic cases, up to and including complete suppression with perpendicular magnetic fields. We show this is true regardless of the local particle arrangement/disorder (even in “worst case” scenarios where the particle arrangement is totally random), and regardless of the “neighbor number” in the spline. For some cases of great astrophysical interest, e.g. diffusion across a moving contact discontinuity which is not aligned with the grid, these methods (by virtue of being Lagrangian and mesh-free) may exhibit substantially reduced numerical diffusion compared to non-moving, grid-based codes (e.g. AMR methods) at the same resolution. The MFM/MFV methods are able to capture subtle instabilities driven by anisotropic diffusion (e.g. the magneto-thermal and heat-flux driven buoyancy instabilities, and Hall MRI).

In the most popular (what we call “standard”) SPH formulation, we obtain good solutions for isotropic diffusion. However, we confirm the conclusions from Petkova & Springel (2009) and Arth et al. (2014) that this discretization appears ill-suited to anisotropic problems. This relates to the fact that pair-wise differences are assumed to define gradients along the line connecting particle centers of mass; this leads to order-unity systematic offsets (i.e. qualitatively incorrect solutions) which limit the maximum anisotropic suppression to a modest factor  $\sim 5$  and artificially suppress parallel diffusion. We stress that these errors *do not converge away* with resolution or neighbor number. Although it is possible to subtract off the “average” systematic error terms (the “error-corrected” formulation), and this appears to help in some specific problems, this renders the scheme numerically unstable, so certain particle configurations can produce rapidly-growing errors and unphysical solutions. Similar stability problems arise in alternative (e.g. “gradients of gradients”) formulations of SPH.

We show that these errors in SPH can be eliminated by (1) replacing the standard zeroth-order inconsistent SPH gradient estimator with the higher-order consistent, moving-least-squares estimator from our MFM method, (2) rewriting the SPH equations in Godunov form, and (3) stabilizing the resulting fluxes by solving a flux-limited Riemann problem between particles. The resulting “integral-Godunov” SPH is essentially identical to our MFM/MFV methods up to a different definition of the “faces” between elements, and so (unsurprisingly) gives similarly accurate results. However, we caution that when coupled to the dynamics, the usual SPH errors (e.g. zeroth-order reconstruction and partition errors, and excessive artificial diffusivity) from the (unmodified) SPH-MHD equations still appear, and corrupt our test problems involving e.g. Braginskii viscosity, the MTI/HBI, and Hall MRI.

The particular form we adopt for the flux-limited Riemann problem is non-trivial, and should be useful for other explicit anisotropic diffusion methods. Stabilizing these methods without introducing excessive numerical diffusion is challenging, especially in irregular/unstructured meshes or mesh-free configurations. The method we propose has the advantage that it trivially generalizes to arbitrarily high-order (and complicated) gradient estimators and slope-limiters, as well as higher-order reconstruction of the gradients at the faces (we simply replace the left and right states in Eqs. 7-11 with their appropriate values); it also admits arbitrarily complex tensors for both the diffusivity and diffused quantities (as opposed to many methods which are specific to scalar diffusion). And the flux computation is pair-wise and negligible in cost compared to the MHD Riemann problem solution. It therefore is of

interest not just to mesh-free methods but also moving-mesh and AMR methods. The major dis-advantage of our method is that it does not trivially generalize for implicit solvers (see Appendix A). This is a subject that merits investigation in future work, since implicit methods can often provide a large speed boost to certain types of problems. However, the methods here are amenable to significant acceleration via super-timestepping, which can provide a comparable speedup as described in Appendix B.

## ACKNOWLEDGMENTS

We thank Eliot Quataert for several helpful suggestions of interesting test problems. Support for PFH was provided by the Gordon and Betty Moore Foundation through Grant #776 to the Caltech Moore Center for Theoretical Cosmology and Physics, an Alfred P. Sloan Research Fellowship, NASA ATP Grant NNX14AH35G, and NSF Collaborative Research Grant #1411920. Numerical calculations were run on the Caltech compute cluster “Zwicky” (NSF MRI award #PHY-0960291) and allocation TG-AST130039 granted by the Extreme Science and Engineering Discovery Environment (XSEDE) supported by the NSF.

## REFERENCES

- Abel, T. 2011, *MNRAS*, 413, 271
- Agertz, O., et al. 2007, *MNRAS*, 380, 963
- Alexiades, V., Amiez, G., & Gremaud, P. A. 1996, *Communications in Numerical Methods in Engineering*, 12, 31
- Arth, A., Dolag, K., Beck, A. M., Petkova, M., & Lesch, H. 2014, *MNRAS*, submitted, arXiv:1412.6533
- Bai, X.-N. 2011, *ApJ*, 739, 50
- Balbus, S. A. 2000, *ApJ*, 534, 420
- . 2003, *ARA&A*, 41, 555
- Bauer, A., & Springel, V. 2012, *MNRAS*, 423, 3102
- Brookshaw, L. 1985, *Proceedings of the Astronomical Society of Australia*, 6, 207
- Chan, T. K., Kereš, D., Oñorbe, J., Hopkins, P. F., Muratov, A. L., Faucher-Giguère, C.-A., & Quataert, E. 2015, *MNRAS*, 454, 2981
- Choi, E., Kim, J., & Wiita, P. J. 2009, *ApJS*, 181, 413
- Cleary, P. W., & Monaghan, J. J. 1999, *Journal of Computational Physics*, 148, 227
- Cullen, L., & Dehnen, W. 2010, *MNRAS*, 408, 669
- Dehnen, W., & Aly, H. 2012, *MNRAS*, 425, 1068
- Dilts, G. A. 1999, *International Journal for Numerical Methods in Engineering*, 44, 1115
- Dolag, K., & Stasyszyn, F. 2009, *MNRAS*, 398, 1678
- Duffell, P. C., & MacFadyen, A. I. 2011, *ApJS*, 197, 15
- . 2014, *MNRAS*, in press, arxiv:1407.7300
- Español, P., & Revenga, M. 2003, *Phys. Rev. E*, 67, 026705
- Faucher-Giguère, C.-A., Hopkins, P. F., Keres, D., Muratov, A. L., Quataert, E., & Murray, N. 2015, *MNRAS*, 449, 987
- Flock, M., Dzyurkevich, N., Klahr, H., Turner, N. J., & Henning, T. 2011, *ApJ*, 735, 122
- Gaburov, E., Johansen, A., & Levin, Y. 2012, *ApJ*, 758, 103
- Gaburov, E., & Nitadori, K. 2011, *MNRAS*, 414, 129
- Gao, Z., & Wu, J. 2013, *Journal of Computational Physics*, 250, 308
- García-Senz, D., Cabezón, R. M., & Escartín, J. A. 2012, *A&A*, 538, A9
- Gnedin, N. Y., & Abel, T. 2001, *New Astronomy*, 6, 437
- Guan, X., & Gammie, C. F. 2008, *ApJS*, 174, 145
- Gurski, K. F., & O’Sullivan, S. 2010, in *American Institute of Physics Conference Series*, Vol. 1281, American Institute of Physics Conference Series, ed. T. E. Simos, G. Psihoyios, & C. Tsitouras, 761–764
- Hahn, O., Teyssier, R., & Carollo, C. M. 2010, *MNRAS*, 405, 274
- Harten, A., Lax, P., & van Leer. 1983, *SIAM Reviews*, 25, 35
- Heitmann, K., et al. 2008, *Computational Science and Discovery*, 1, 015003
- Hopkins, P. F. 2013, *MNRAS*, 428, 2840
- . 2015a, *MNRAS*, in press, arXiv:1509.07877
- . 2015b, *MNRAS*, 450, 53
- Hopkins, P. F., Keres, D., Onorbe, J., Faucher-Giguère, C.-A., Quataert, E., Murray, N., & Bullock, J. S. 2014, *MNRAS*, 445, 581
- Hopkins, P. F., & Raives, M. J. 2016, *MNRAS*, 455, 51
- Hu, C.-Y., Naab, T., Walch, S., Moster, B. P., & Oser, L. 2014, *MNRAS*(arXiv:1402.1788)
- Kannan, R., Springel, V., Pakmor, R., Marinacci, F., & Vogelsberger, M. 2015, *MNRAS*, submitted, arXiv:1512.03053
- Kitsionas, S., et al. 2009, *A&A*, 508, 541
- Kuhnert, J. 2003, in *Lecture Notes in Computational Science and Engineering*, Vol. 26, *Meshfree Methods for Partial Differential Equations*, ed. M. Griebel & M. Schweitzer (Springer Berlin Heidelberg), 239–249
- Lanson, N., & Vila, J.-P. 2008a, *SIAM J. Numer. Anal.*, 46, 1912
- . 2008b, *SIAM J. Numer. Anal.*, 46, 1935
- LeVeque, R. J. 1998, *Journal of Computational Physics*, 146, 346
- Luo, H., Baum, J. D., & Löhner, R. 2008, *Journal of Computational Physics*, 227, 8875
- Ma, X., Hopkins, P. F., Faucher-Giguère, C.-A., Zolman, N., Muratov, A. L., Kereš, D., & Quataert, E. 2016, *MNRAS*, 456, 2140
- Ma, X., Kasen, D., Hopkins, P. F., Faucher-Giguère, C.-A., Quataert, E., Kereš, D., & Murray, N. 2015, *MNRAS*, 453, 960
- Maior, U., Dotti, M., Petkova, M., Perego, A., & Volonteri, M. 2013, *ApJ*, 767, 37
- Maron, J. L., & Howes, G. G. 2003, *ApJ*, 595, 564
- McCourt, M., Parrish, I. J., Sharma, P., & Quataert, E. 2011, *MNRAS*, 413, 1295
- Meyer, C. D., Balsara, D. S., & Aslam, T. D. 2012, *MNRAS*, 422, 2102
- . 2014, *Journal of Computational Physics*, 257, 594
- Mocz, P., Vogelsberger, M., Pakmor, R., Genel, S., Springel, V., & Hernquist, L. 2015, *MNRAS*, 452, 3853
- Mocz, P., Vogelsberger, M., Sijacki, D., Pakmor, R., & Hernquist, L. 2014, *MNRAS*, 437, 397
- Morris, J. P. 1996, *Publications of the Astronomical Society of Australia*, 13, 97
- Muñoz, D. J., Springel, V., Marcus, R., Vogelsberger, M., & Hernquist, L. 2013, *MNRAS*, 428, 254
- Müller, E., & Steinmetz, M. 1995, *Computer Physics Communications*, 89, 45
- Muratov, A. L., Kereš, D., Faucher-Giguère, C.-A., Hopkins, P. F., Quataert, E., & Murray, N. 2015, *MNRAS*, 454, 2691
- Oñate, E., Idelsohn, S., Zienkiewicz, O. C., & Taylor, R. L. 1996, *International Journal for Numerical Methods in Engineering*, 39, 3839
- Oñorbe, J., Boylan-Kolchin, M., Bullock, J. S., Hopkins, P. F., Kereš, D., Faucher-Giguère, C.-A., Quataert, E., & Murray, N. 2015, *MNRAS*, 454, 2092
- O’Shea, B. W., Nagamine, K., Springel, V., Hernquist, L., & Norman, M. L. 2005, *ApJS*, 160, 1
- Pakmor, R., Springel, V., Bauer, A., Mocz, P., Muñoz, D. J.,

Ohlmann, S. T., Schaal, K., & Zhu, C. 2016, MNRAS, 455, 1134  
 Parrish, I. J., & Quataert, E. 2008, ApJL, 677, L9  
 Parrish, I. J., & Stone, J. M. 2005, ApJ, 633, 334  
 Parrish, I. J., Stone, J. M., & Lemaster, N. 2008, ApJ, 688, 905  
 Peery, K., & Imlay, S. 1988, Blunt-body flow simulations (American Institute of Aeronautics and Astronautics), 2904+  
 Petkova, M., & Maio, U. 2012, MNRAS, 422, 3067  
 Petkova, M., & Springel, V. 2009, MNRAS, 396, 1383  
 —. 2011a, MNRAS, 415, 3731  
 —. 2011b, MNRAS, 412, 935  
 Price, D. J. 2012, Journal of Computational Physics, 231, 759  
 Price, D. J., & Bate, M. R. 2008, MNRAS, 385, 1820  
 Price, D. J., & Federrath, C. 2010, MNRAS, 406, 1659  
 Quataert, E. 2008, ApJ, 673, 758  
 Read, J. I., Hayfield, T., & Agertz, O. 2010, MNRAS, 405, 1513  
 Ritchie, B. W., & Thomas, P. A. 2001, MNRAS, 323, 743  
 Rosdahl, J., & Teyssier, R. 2015, MNRAS, 449, 4380  
 Rosswog, S. 2014, arXiv e-print: 1405.6034  
 Rosswog, S., & Price, D. 2007, MNRAS, 379, 915  
 Sales, L. V., Marinacci, F., Springel, V., & Petkova, M. 2013, MNRAS, in press, arXiv:1310.7572  
 Sano, T., & Stone, J. M. 2002, ApJ, 570, 314  
 Sharma, P., Colella, P., & Martin, D. F. 2010, SIAM J. Sci. Comput., 32, 3564  
 Sharma, P., & Hammett, G. W. 2007, Journal of Computational Physics, 227, 123  
 —. 2011, Journal of Computational Physics, 230, 4899  
 Sijacki, D., & Springel, V. 2006, MNRAS, 371, 1025  
 Sijacki, D., Vogelsberger, M., Keres, D., Springel, V., & Hernquist, L. 2012, MNRAS, 424, 2999  
 Simon, J. B., Hawley, J. F., & Beckwith, K. 2011, ApJ, 730, 94  
 Simon, J. B., Lesur, G., Kunz, M. W., & Armitage, P. J. 2015, MNRAS, 454, 1117  
 Smagorinsky, J. 1963, Monthly Weather Review, 91, 99  
 Springel, V. 2005, MNRAS, 364, 1105  
 Springel, V. 2010, MNRAS, 401, 791  
 Springel, V., & Hernquist, L. 2002, MNRAS, 333, 649  
 Stone, J. M., Gardiner, T. A., Teuben, P., Hawley, J. F., & Simon, J. B. 2008, ApJS, 178, 137  
 Tasker, E. J., & Bryan, G. L. 2008, ApJ, 673, 810  
 Tricco, T. S., & Price, D. J. 2012, Journal of Computational Physics, 231, 7214  
 Tsukamoto, Y., Iwasaki, K., & Inutsuka, S.-i. 2013, MNRAS, 434, 2593  
 Tsukamoto, Y., Iwasaki, K., Okuzumi, S., Machida, M. N., & Inutsuka, S. 2015a, ApJL, 810, L26  
 —. 2015b, MNRAS, 452, 278  
 Uhlig, M., Pfrommer, C., Sharma, M., Nath, B. B., Enßlin, T. A., & Springel, V. 2012, MNRAS, 423, 2374  
 Wardle, M. 2007, Astrophysics and Space Science, 311, 35  
 Wurster, J., Price, D., & Ayliffe, B. 2014, MNRAS, 444, 1104  
 Wurster, J., Price, D. J., & Bate, M. R. 2016, MNRAS, 457, 1037  
 Zingale, M., et al. 2002, ApJS, 143, 539

## APPENDIX A: IMPLICIT METHODS

In the main text we solve the diffusion equations explicitly. Qualitatively speaking, we update  $\mathbf{U}$  according to

$$(\mathbf{VU})^{n+1} = (\mathbf{VU})^n + \Delta t \frac{d(\mathbf{VU})^{n+1/2}}{dt} \quad (\text{A1})$$

where  $n$  refers to the timestep and  $n + 1/2$  refers to drifting all quantities to a half-timestep before calculating  $d(\mathbf{VU})/dt$  (see Paper I for details).

The explicit solver has the advantages of computational simplicity, extension to high-order gradient operators/reconstruction methods, allowing non-linear flux limiters, and trivially generalizing to hierarchical adaptive timesteps as we use in our code (akin to “sub-cycling”). However, the disadvantage is that it requires a timestep limit of the form in Eq. 15 (quadratic in the resolution). In some situations this can become extremely small; in these cases, implicit methods are popular. In the implicit case, we take

$$(\mathbf{VU})^{n+1} = (\mathbf{VU})^n + \Delta t \frac{d(\mathbf{VU})^{n+1}}{dt} \quad (\text{A2})$$

Petkova & Springel (2009) show how the “standard” SPH method here can be solved implicitly. Consider a scalar  $\mathbf{q} = q = \zeta U$ ; we use Eq. 19 for  $d(\mathbf{VU})/dt$ , and after some re-arranging, Eq. A2 can be cast in the form:

$$(\mathbf{VU})_a^{n+1} = (\mathbf{VU})_a^n + \sum_b \bar{\omega}_{ab} \left[ \frac{\zeta_b (\mathbf{VU})_b^{n+1}}{V_b} - \frac{\zeta_a (\mathbf{VU})_a^{n+1}}{V_a} \right] \quad (\text{A3})$$

This is linear equation so if we treat  $(\mathbf{VU})$  as a vector with elements  $(\mathbf{VU})_a$ , we can write it in matrix form:

$$\mathbf{M} \cdot (\mathbf{VU})^{n+1} = (\mathbf{VU})^n \quad (\text{A4})$$

$$M_{ab} \equiv \delta_{ab} - \frac{\zeta_b}{V_b} \left( \bar{\omega}_{ab} - \bar{\omega}_b^S \delta_{ab} \right) \quad (\text{A5})$$

$$\bar{\omega}_{ab} \equiv \Delta t \frac{m_a m_b}{\rho_a \rho_b} \frac{\bar{W}_{ab}}{|\mathbf{x}_{ab}|} [\hat{\mathbf{x}}_{ab}^T (\mathbf{K}_a + \mathbf{K}_b) \hat{\mathbf{x}}_{ab}] \quad (\text{A6})$$

$$\bar{\omega}_a^S \equiv \sum_c \bar{\omega}_{ac} \quad (\text{A7})$$

where  $\delta_{ab}$  is the Kronecker delta. So updating  $(\mathbf{VU})$  requires a global sparse-matrix inversion. We have implemented a conjugate-gradient inversion identical to Petkova & Springel (2009) to solve the implicit equation over all particles in a global timestep. Using this, we have verified that all of our conclusions regarding accuracy, stability, and systematic errors of the standard SPH method(s) are identical regardless of whether we solve the equations explicitly or implicitly.

For our MFM/MFV/IG-SPH methods, deriving an implicit method is more challenging. If we simplify by using a first-order reconstruction of  $\nabla \otimes \mathbf{q}$  (with corresponding limiters), and (for now) neglect the extra diffusion terms from the Riemann problem, and assume a scalar  $\mathbf{q}$ , then Eq. 3 for  $d(\mathbf{VU})/dt$  gives us

$$(\mathbf{VU})_a^{n+1} = (\mathbf{VU})_a^n + \frac{\Delta t}{2} \sum_b \left( \mathbf{K}_a \langle \nabla q \rangle_a^{n+1} + \mathbf{K}_b \langle \nabla q \rangle_b^{n+1} \right) \cdot \theta_{ab} \mathbf{A}_{ab} \quad (\text{A8})$$

where  $\theta_{ab}$  is the limiter function based on comparing the implied flux here to the “direct flux” per Eq. 14. Combining this with Eq. 4 for the gradient estimators, re-arranging and simplifying, we obtain

$$\mathbf{M} \cdot (\mathbf{VU})^{n+1} = (\mathbf{VU})^n \quad (\text{A9})$$

$$M_{ab} \equiv \delta_{ab} + \frac{\Delta t}{2} \frac{\zeta_b}{V_b} \left[ \mathbf{K}_b \boldsymbol{\mu}_b^S \cdot \left( \tilde{\mathbf{A}}_{ab} + \tilde{\mathbf{A}}_b^S \delta_{ab} \right) + \sum_c \mathbf{K}_c \boldsymbol{\mu}_{cb} \cdot \left( \tilde{\mathbf{A}}_{ac} - \tilde{\mathbf{A}}_c^S \delta_{ac} \right) \right] \quad (\text{A10})$$

$$\tilde{\mathbf{A}}_{ab} \equiv \theta_{ab} \mathbf{A}_{ab} \quad , \quad \boldsymbol{\mu}_b \equiv \beta_a \mathbf{W}_a^{-1} \mathbf{x}_{ba} \omega_b(\mathbf{x}_a) \quad (\text{A11})$$

$$\tilde{\mathbf{A}}_a^S \equiv \sum_c \tilde{\mathbf{A}}_{ac} \quad , \quad \boldsymbol{\mu}_a^S \equiv \sum_c \boldsymbol{\mu}_{ac} \quad (\text{A12})$$

where  $\omega$  and  $\mathbf{W}^{-1}$  are defined in Eq. 4, and  $\beta$  is the slope-limiter for  $\langle \nabla \otimes \mathbf{q} \rangle$  (see Paper I). Now, add the diffusive terms from the Riemann problem,  $\mathbf{F} \rightarrow \mathbf{F} + \mathbf{F}_{\text{diss}}$  where  $\mathbf{F}_{\text{diss}} = \alpha \lambda (\mathbf{U}_R - \mathbf{U}_L) = \alpha_{ab} \lambda_{ab} [u_a - u_b + (\eta_{ab}/2)(\nabla u_a + \nabla u_b) \cdot \mathbf{x}_{ba}]$  if we use our default second-order reconstruction of the  $\mathbf{U}_R$  and  $\mathbf{U}_L$ . Here  $\lambda = |v_R - v_L|/2 + c_{\text{fast}}$  and  $\eta_{ab}$  is the appropriate limiter for the  $U_R, U_L$  reconstruction, both as defined in the text. This gives us

$$\mathbf{M} \rightarrow \mathbf{M} + \mathbf{M}^{\text{diss}} \quad (\text{A13})$$

$$\begin{aligned} M_{ab}^{\text{diss}} \equiv & -\frac{\Delta t}{2V_b} \left[ 2 \left( \varphi_{ab} - \varphi_b^S \delta_{ab} \right) + \boldsymbol{\mu}_b^S \cdot \left( \boldsymbol{\Lambda}_{ab} + \boldsymbol{\Lambda}_b^S \delta_{ab} \right) \right. \\ & \left. - \sum_c \boldsymbol{\mu}_{cb} \cdot \left( \boldsymbol{\Lambda}_{ac} + \boldsymbol{\Lambda}_c^S \delta_{ac} \right) \right] \end{aligned} \quad (\text{A14})$$

$$\varphi_{ab} \equiv \alpha_{ab} \lambda_{ab} |\tilde{\mathbf{A}}|_{ab}, \quad \boldsymbol{\Lambda}_{ab} \equiv \eta_{ab} \varphi_{ab} \mathbf{x}_{ba} \quad (\text{A15})$$

$$\varphi_a^S \equiv \sum_c \varphi_{ac}, \quad \boldsymbol{\Lambda}_a^S \equiv \sum_c \boldsymbol{\Lambda}_{ac} \quad (\text{A16})$$

The difference between MFM and IG-SPH simply amounts to the appropriate value for  $\boldsymbol{\Lambda}_{ab}$ .

If the limiter functions  $\theta_{ab}$ ,  $\eta_{ab}$ ,  $\alpha_{ab}$ , and  $\beta_a$  were independent of  $(\mathbf{V}\mathbf{U})$ , then we could again perform a simple sparse-matrix inversion to update  $(\mathbf{V}\mathbf{U})$ . Obviously even in this limit, the matrix terms are more complicated than standard SPH: note the extra summations over the index “ $c$ ” that appear, which owe to the higher-order gradient estimator we adopt and cannot be eliminated without lowering the order of the gradient approximation. But the real problem is that the higher-order accuracy and stability of our MFM/MFV/IG-SPH methods depends on the limiters being *non-linear* functions of *both*  $\mathbf{U}_{a,b}$  and  $\nabla \otimes \mathbf{q}_{a,b}$  (itself a sum over  $\mathbf{U}_{a,b}$ ). Of course, non-linear global elliptical equations can be solved, but using an iterative root-finding method to solve for  $(\mathbf{V}\mathbf{U})$ , we would have to repeat the summation over  $\mathbf{U}$  to determine  $\nabla \otimes \mathbf{q}_{a,b}$  and re-compute the limiter functions between each iteration. Combined with a global timestep, this would make the implicit solver much more expensive than sub-cycling our explicit solver (defeating the purpose).

In the limit where the problem is sufficiently smooth, well-resolved, and there is good particle order,  $\theta, \eta, \beta \rightarrow 1$  and  $\alpha \rightarrow 0$ . Adopting these values and implementing the sparse matrix inversion, we are able to confirm our conclusions for the few test problems that satisfy these criteria. However, with these values fixed, the method is numerically unstable. We can stabilize the method for problems with unresolved gradients (still assuming good particle order) by taking  $\theta, \beta, \alpha \rightarrow 1, \eta \rightarrow 0$ , but this produces excessive numerical diffusion, especially at low resolution. Unfortunately, we see no obvious way to achieve the combination of accuracy and stability in the text (given the method studied here) without involving non-linear terms in  $\nabla \otimes \mathbf{q}$ , which are prohibitive for most implicit methods. However, it is possible that a semi-implicit method similar to the one in Sharma & Hammett (2011) could be implemented, where a subset of the flux components which do not require strong limiters are solved implicitly while the others (where the limiters apply) are updated explicitly.

## APPENDIX B: SUPER-TIMESTEPPING

Another method to allow larger timesteps in explicit methods for elliptic/parabolic equations is so-called “super-timestepping” (see Alexiades et al. 1996; Gurski & O’Sullivan 2010; Meyer et al. 2012, 2014, and references therein).

A super-timestep  $\Delta t_s$  is composed of  $N$  sub-steps  $\delta t_j$

$$\Delta t_s = \sum_{j=1}^N \delta t_j \quad (\text{B1})$$

The diffusion equations are calculated and updated as usual on each sub-step  $\delta t_j$ , however, these are essentially Runge-Kutta sub-steps in the sense that stability is not guaranteed after any individual sub-step  $\delta t_j$ , but *only* on the super-step  $\Delta t_s$ .

Alexiades et al. (1996) show that the optimal timesteps which satisfy the necessary stability conditions on  $\Delta t_s$  and simultaneously maximize  $\Delta t_s$  for a given  $N$  are given by

$$\delta t_j = \Delta t_{\text{expl}} \left[ (1 + \nu) - (1 - \nu) \cos \left( \frac{\pi(2j-1)}{2N} \right) \right]^{-1} \quad (\text{B2})$$

where  $\Delta t_{\text{expl}}$  is our usual explicit timestep given by Eq. 15 and  $0 < \nu < \lambda_{\text{min}}/\lambda_{\text{max}}$  (where  $\lambda_{\text{min}}$  and  $\lambda_{\text{max}}$  are the smallest and largest eigenvalues of the diffusion equation). As  $\nu \rightarrow 0$ , the total time  $\Delta t_s$  covered by the same number  $N$  of substeps (and computations) increases, with the limit  $\Delta t_s \rightarrow N^2 \Delta t_{\text{expl}}$  as  $\nu \rightarrow 0$ . Thus this method can provide a speedup of up to a factor  $N$ .

This is trivial to implement in explicit methods with a global timestep, and we have done so here. Although all problems shown in the text use the standard, non-optimized explicit timestep  $\Delta t_{\text{expl}}$ , we have re-run all of them enforcing a global timestep and using the super-timestepping scheme with varying  $N$  and  $\nu$ . Care is needed, since overly-aggressive timestepping can lead to a loss of accuracy even while maintaining stability (see discussion in § C). In practice, we find  $N \sim 5 - 10$  and  $\nu \sim 0.04$  give substantial speed-ups (factor  $\sim 2.5 - 3$  on the problems here) without any measurable loss of accuracy (consistent with the studies in Alexiades et al. 1996; Choi et al. 2009 and Tsukamoto et al. 2013, who show good accuracy is maintained for  $\nu \gtrsim 1/N^{1/2}$ ).

Moreover, it is straightforward to generalize this to our individual timestepping scheme. In this scheme, particles have independent timesteps but are discretized into hierarchical powers-of-two timebins (see Paper I and Springel 2005); this ensures they remain synchronized. If we take each  $\delta t_j$  and “round down” the nearest (smaller) power-of-two bin, it is straightforward to show that the stability condition in Alexiades et al. (1996) is still satisfied (more easily, in fact). The tradeoff is that the timesteps are no longer quite “optimal” (not as large as possible). However, for careful choices of  $N$  and  $\nu$  (such as the values above), the difference in the super-step  $\Delta t_s$  (the sum of the  $\delta t_j$ ) is only  $\sim 10\%$  below optimal.

Note that this is a first-order time integration scheme, which makes it particularly easy to implement. Still greater accuracy may be achieved with higher-order schemes following Meyer et al. (2012, 2014), but we have not experimented with these.

## APPENDIX C: TIMESTEP LIMITS WITH SUPER-TIMESTEPPING OR IMPLICIT SOLVERS

With either implicit methods or super-timestepping, although formal stability is guaranteed for large time-steps, accuracy is not. For any test problem, we can simply vary the timestep until a desired accuracy is reached. However for more general problems, it is useful to have a more general timestep constraint.

Regardless of the diffusion problem, MHD must obey the usual CFL condition  $\Delta t < C_{\text{CFL}} \Delta x/v_{\text{sig}}$  (where  $v_{\text{sig}}$  is the standard signal velocity accounting for particle relative motions and their fastest wavespeeds). Additional physics (e.g. gravity, radiation, cooling) come with their own timestep constraints. Note that, for hyperbolic equations, we cannot circumvent these conditions

using either of the acceleration schemes above; they are always enforced.

There is no rigorous equivalent condition for the diffusion equation with implicit/super-timestepped solvers, but as pointed out by many authors (e.g. Choi et al. 2009; Gurski & O’Sullivan 2010; Tsukamoto et al. 2013), motivated by hyperbolic problems, we can define an effective diffusive signal speed  $v_{\text{diff}} \sim \|\mathbf{K}\| \|\nabla \otimes \mathbf{q}\| / \|\mathbf{q}\|$ . Using this to define an analogous Courant condition on the super/implicit timestep:

$$\Delta t_{\text{implicit/super}} < C_{\text{CFL}} \Delta x \frac{\|\mathbf{q}\|}{\|\mathbf{K}\| \|\nabla \otimes \mathbf{q}\|} \quad (\text{C1})$$

we find reasonably good accuracy so long as  $C_{\text{CFL}} < 0.5$ . For more details we refer to Sharma et al. (2010) who rigorously demonstrate that such a criterion is the correct one for regimes where the diffusion equation behaves advectively (e.g. cosmic ray streaming, or our variable-diffusivity test problem).

Note that when there are un-resolved gradients, this reduces to the usual explicit timestep-limiter,  $\Delta t < \Delta x^2 / \|\mathbf{K}\|$ , as we might expect.<sup>14</sup> When the gradients are well-resolved, however, larger timesteps are allowed: for super-timestepping, this amounts to a speedup by a factor  $\sim L_{\text{grad}} / (N \Delta x)$  where  $N$  is the number of sub-steps and  $L_{\text{grad}} = \|\mathbf{q}\| / \|\nabla \otimes \mathbf{q}\|$  is the gradient scale length. In practice, for most of the test problems in this paper, this translates to a maximum speedup of a factor of  $\sim 3$  in super-timestepping before a noticeable loss of accuracy appears. Given the large overhead of the implicit methods, for the few cases where we can use them (e.g. “standard” SPH), we actually see relatively little speedup (factor  $< 2$ ). However, if we considered the same problems, in stages with *resolved* gradients, at much higher resolution, the difference between the simple explicit method used in the text and either implicit or super-timestepped methods should grow accordingly.

<sup>14</sup> On some problems – for example the diffusing sheet with perpendicular fields, implicit methods remain accurate even with much larger timesteps compared to Eq. C1. However, the only cases we find this is true are ones where the solution is steady-state or equilibrium (in which case arbitrarily long timesteps should not, in principle, be problematic). For all realistic problems we consider which feature actual dynamics, a criterion like Eq. C1 is needed to maintain accuracy.